Python-based tools for characterizing geosynchronous satellite behavior and evaluating maneuver prediction techniques

by

Haley Elizabeth Solera

Submitted to the Department of Aeronautics and Astronautics
in partial fulfillment of the requirements for the degree of

Master of Science in Aeronautics and Astronautics

at the

MASSACHUSETTS INSTITUTE OF TECHNOLOGY

May 2023

Authored by: Haley Elizabeth Solera
Department of Aeronautics and Astronautics
May 23, 2023

Certified by: Richard Linares
Associate Professor of Aeronautics and Astronautics
Thesis Supervisor

Accepted by: Jonathan P. How
R. C. Maclaurin Professor of Aeronautics and Astronautics
Chair, Graduate Program Committee

Python-based tools for characterizing geosynchronous satellite behavior and evaluating maneuver prediction techniques

by

Haley Elizabeth Solera

Submitted to the Department of Aeronautics and Astronautics
on May 23, 2023, in partial fulfillment of the
requirements for the degree of
Master of Science in Aeronautics and Astronautics

Abstract

Geosynchronous (GEO) satellites maneuver frequently to maintain their Earth-relative position despite drift incurred from natural perturbations, but quantifying their diverse maneuver patterns can be challenging. Even for individual satellites, between one station-keeping cycle and the next, the frequency, magnitude, and direction of maneuvers can change. Additionally, there is very little accountability among operators to disclose detailed mission objectives and precise orbital data or to adhere to operational guidelines. This complicates the process of characterizing station-keeping control objectives, predicting maneuvers, and recognizing the early signs of a shift in a satellite's pattern of life (PoL). Characterizing PoLs for a diverse range of GEO satellites can help to contextualize historic on-orbit behaviors and behavior patterns, cultivate generalized maneuver prediction on a large scale, and help future behaviors to be quickly identified as anomalous, nominal, or indicative of a certain mission objective. This work presents two Python tools designed to address these challenges by improving the general accessibility of broad-scale PoL characterization and predictive aspects of Space Situational Awareness (SSA).

First, a nomenclature for a generalizable PoL model is proposed, and a simple algorithm is introduced to enable PoL characterization according to this model. The algorithm is shown to efficiently process a large number of satellite histories by isolating PoL shifts - called nodes - even from sparse or low-precision position histories like collections of two-line-element (TLE) sets. Then, a second simulation tool is described and demonstrated to evaluate probabilistic maneuver prediction models in context of physical viewing constraints determined by user-defined surveillance scenarios. This work explores the potential of both tools to address data accessibility challenges and facilitate GEO satellite behavior characterization in order to foster a more cohesive and communicative SSA research community.

Thesis Supervisor: Richard Linares
Title: Associate Professor of Aeronautics and Astronautics

Acknowledgments

This work was made possible by the many incredible friends, mentors, and colleagues who have supported me in recent years. Firstly, I would like to extend my sincere thanks to my advisor, Professor Richard Linares, for his guidance over the past two years and for affording me the flexibility and freedom to discover my research interests in a new field. I would like to thank all of my colleagues at the Astrodynamics, Space Robotics, and Controls Laboratory for their kindness and mentorship, and special thanks to Thomas G. Roberts for his invaluable contribution in refining my ideas and building my confidence as a researcher. I would also like to express my deepest appreciation for my mentors and colleagues in Group 99 at MIT Lincoln Laboratory for generously welcoming me into their group. To Alexandra Wright, thank you for the advice and considerable amount of time you have invested in me. They were an invaluable influence on this work and the development of my professional interests.

I would like to express my heartfelt gratitude to my grandparents, cousins, aunts, and uncles for their unwavering support, patience, and love all these years. Your belief in me, constant encouragement, and understanding have been the pillars of strength that propelled me forward in moments of doubt and exhaustion. To my parents, I am deeply grateful for the sacrifices you have made, the countless late nights you patiently endured, and the moments you set aside to celebrate my achievements and offer a comforting embrace during setbacks. Many thanks to my friends, near and far. Your presence, whether through words of encouragement, acts of kindness, or a listening ear, has been a source of inspiration and motivation in difficult times. Finally, I gratefully acknowledge the assistance of my service dog, Basil, who worked diligently to keep me safe and healthy throughout the journey of completing this thesis.

This research was sponsored in part by the United States Air Force Research Laboratory and the United States Air Force Artificial Intelligence Accelerator and was accomplished under Cooperative Agreement Number FA8750-19-2-1000. The views and conclusions contained in this document are those of the authors and should not

be interpreted as representing the official policies, either expressed or implied, of the United States Air Force or the U.S. Government. The U.S. Government is authorized to reproduce and distribute reprints for Government purposes notwithstanding any copyright notation herein. This work was also supported by the National GEM Consortium Fellowship Program under Grant No. 1646863.

Contents

List of Figures

List of Tables

Chapter 1

Introduction

Geosynchronous (GEO) satellites maneuver frequently to maintain their Earth-relative position despite drift incurred from natural perturbations, but their maneuver patterns are often difficult to quantify [15]. Even for individual satellites, between one station-keeping cycle and the next, the frequency, magnitude, and direction of maneuvers can change. This diversity complicates the process of characterizing station-keeping control objectives, predicting maneuvers, and recognizing the early signs of a shift in a satellite's pattern of life (PoL) since some understanding of a satellite's nominal behavior is necessary to identify abnormal behavior. This work discusses the implementation of two Python tools designed to improve the general accessibility of broad-scale PoL analysis and the predictive aspects of Space Situational Awareness (SSA). Chapter 1 provides a brief introduction to SSA in the geosynchronous orbital regime, Chapter 2 discusses a simple algorithm for processing large amounts of historical positional data for GEO satellites, and Chapter 3 introduces a tool for evaluating maneuver prediction models in the context of satellite tracking. The implications and further potential of these tools are discussed in Chapter 4.

1.1 Background

1.1.1 Satellite Pattern of Life

In this work, Pattern of Life (PoL) refers to the unique timeline of behaviors displayed by an individual satellite over the course of its life on orbit. Some behaviors - or behavioral modes - are present within the PoLs of a large number of satellites, and if they can be characterized for a sizeable, varied population of active and retired GEO satellites, the resulting PoLs may exhibit trends and provide metrics with which future satellite behaviors can be compared. Contextualizing GEO satellite behaviors and behavior patterns is a necessary step in implementing generalized maneuver prediction on a large scale and can help future behaviors to be quickly identified as anomalous, nominal, or indicative of a certain mission objective [50].

A major component of broad-scale PoL characterization is recognizing behavioral shifts at the macro level. Even though each PoL is unique, its behavioral modes can be sorted into broad categories such as orbit insertion, libration, station-keeping, longitudinal-shifts, or end-of-life (EoL) behaviors [37, 55, 36, 47, 12]. Modes within these categories share general features but may appear to have substantial differences when studied at smaller timescales. For example, periods of orbit insertion look dissimilar for satellites with different propulsion schemes, but they can be classified under the same general mode category. EoL behavioral modes are also highly individual since they are affected by a satellite's maneuverability constraints like remaining fuel or malfunctioning thrusters.

Station-keeping encompasses the largest components of most PoLs in GEO. At the macro level, this class of behaviors includes time periods during which a satellite's periodic motion is centered at a consistent longitude so that it remains within the bounds of a fixed, Earth-relative station. Since there are many maneuver schemes that meet this criterion, there are many possible sub-classes of station-keeping behavioral modes. Therefore, when performing generalized PoL characterization to identify macro-level behavioral modes, it is important to use a method that can identify periods of long-term station-keeping while ignoring minor variations - such as those shown

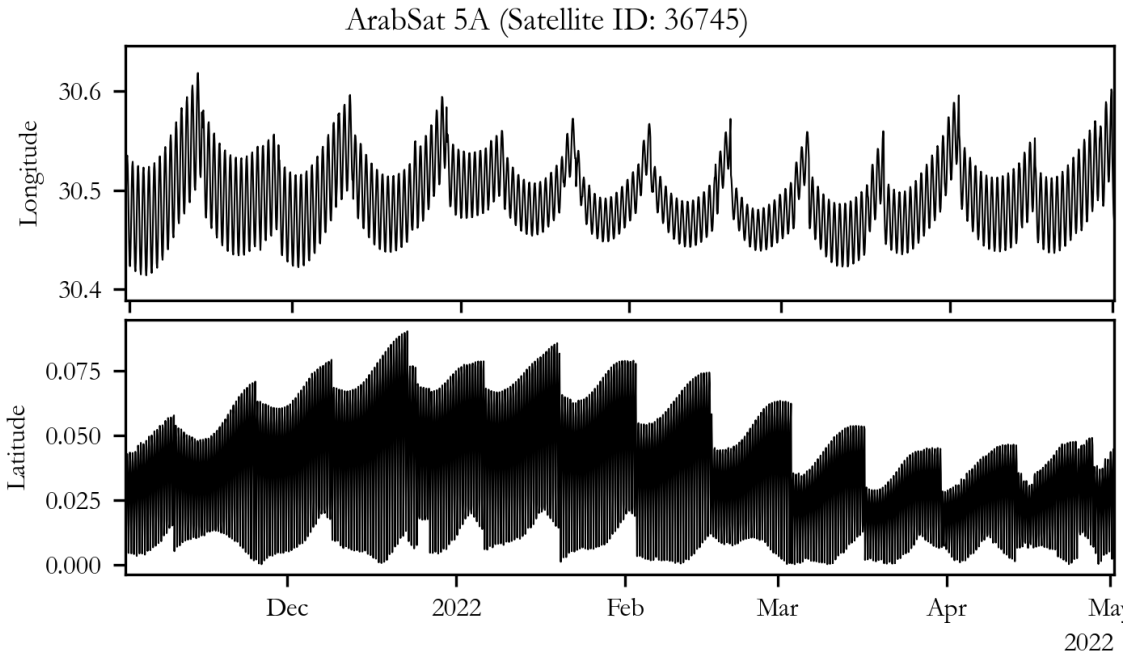

Figure 1-1: **Example of maneuver variability within a station-keeping routine.** Geographic position history for *ArabSat 5A* (Satellite ID: 36745) during a station-keeping behavioral mode. The latitude history shows regular, high-thrust North-South maneuvers every 14 days, but the longitude history is indicative of a much more variable East-West station-keeping routine with high-thrust maneuvers every 11 to 18 days. The satellite's largest gap between East-West station-keeping maneuvers over this period falls in the second half of December 2021.

in Figure 1-1 - that typify most station-keeping routines.

1.1.2 Orbital Slots and Station-Keeping Maneuvers

GEO stations - also referred to as orbital slots - usually encompass a longitudinal range of a few tenths of a degree, though this can vary between operators, mission types, and even regions within the geostationary belt as is the case in Figure 1-2 [43, 8]. They also have a variety of latitudinal ranges. Most station-keeping maneuvers can be categorized as East-West or North-South and adjust a satellite's longitude and inclination respectively. The main thruster burn is along the axis of forward motion for East-West maneuvers and along the transverse axis during North-South maneuvers. Typically, North-South maneuvers require more fuel, so satellites with different mission priorities have different optimizations for North-South maneuver

routines and, as a consequence, different latitudinal ranges [14]. Additionally, North-South maneuvers and routines often change over the course of a satellite's lifetime since the magnitude of the force generated by a satellite's thrusters tends to be less tractable as they age, and fuel constraints become more actionable as a satellite approaches retirement [10].

Propulsion mechanisms are another factor that influences the magnitude, frequency, and consistency of station-keeping maneuvers [54, 39]. Most satellites use chemical thrusters exclusively or hybrid propulsion systems with supplemental Hall Effect thrusters for small, frequent North-South maneuvers. However, electric propulsion systems are becoming more common, and electric thrusters are generally capable of more precise maneuvers than chemical thrusters [32, 23]. As a result, satellites with electric or hybrid propulsion systems may perform multiple station-keeping maneuvers every day while satellites with chemical propulsion systems tend to maneuver a few times a week at most [8, 12]. This leads to a disparity in maneuver magnitudes as well since station-keeping routines with less frequent maneuvers require larger burns to achieve comparable station sizes.

1.1.3 Satellite Tracking

Most automated satellite tracking does not account for routine maneuvers like station-keeping. As is the case in Figure 1-3, satellites often deviate from their expected trajectory between observations, resulting in lost or cross-tagged objects. Maneuver prediction algorithms can help mitigate this problem, but as shown in Figure 1-4, even small variations in maneuver magnitudes and timing can have a significant impact on a satellite's location at the time when it is next observed. Sometimes satellites go days or weeks unobserved, during which time they may have performed any number of maneuvers that changed their orbits.

Not only does the likelihood of a lost or cross-tagged satellite increase with the time between observations; it also increases the closer a satellite operates to other objects. Satellites in clusters operate in close proximity, requiring them to maneuver often and making it more difficult for sensors to distinguish them from one another. Figure

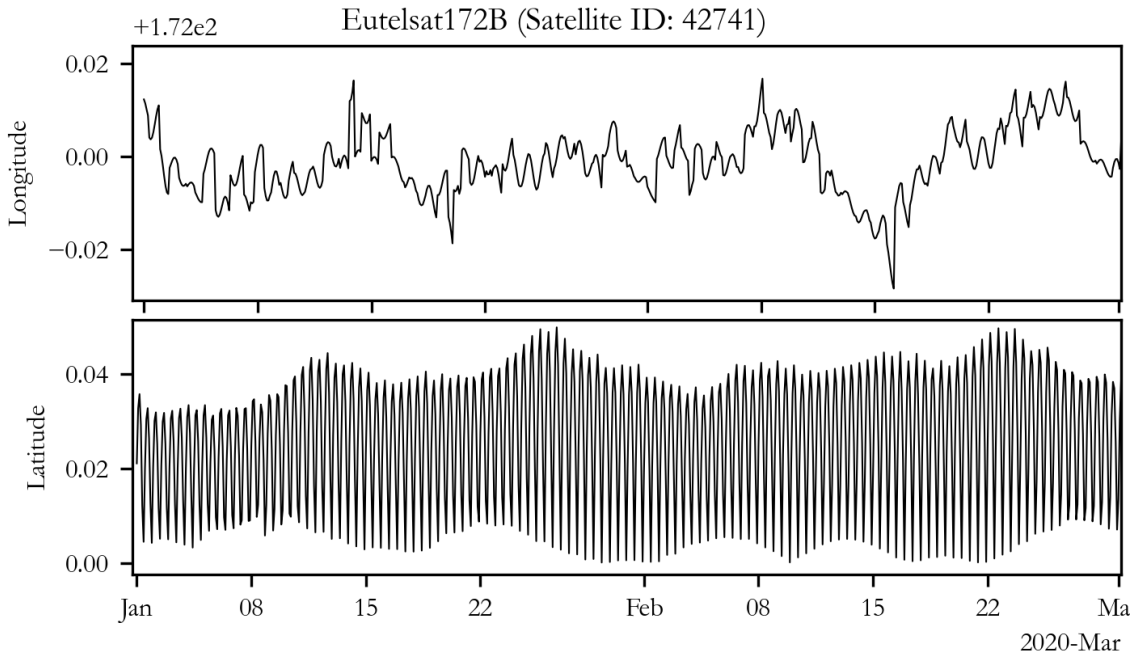

(a)

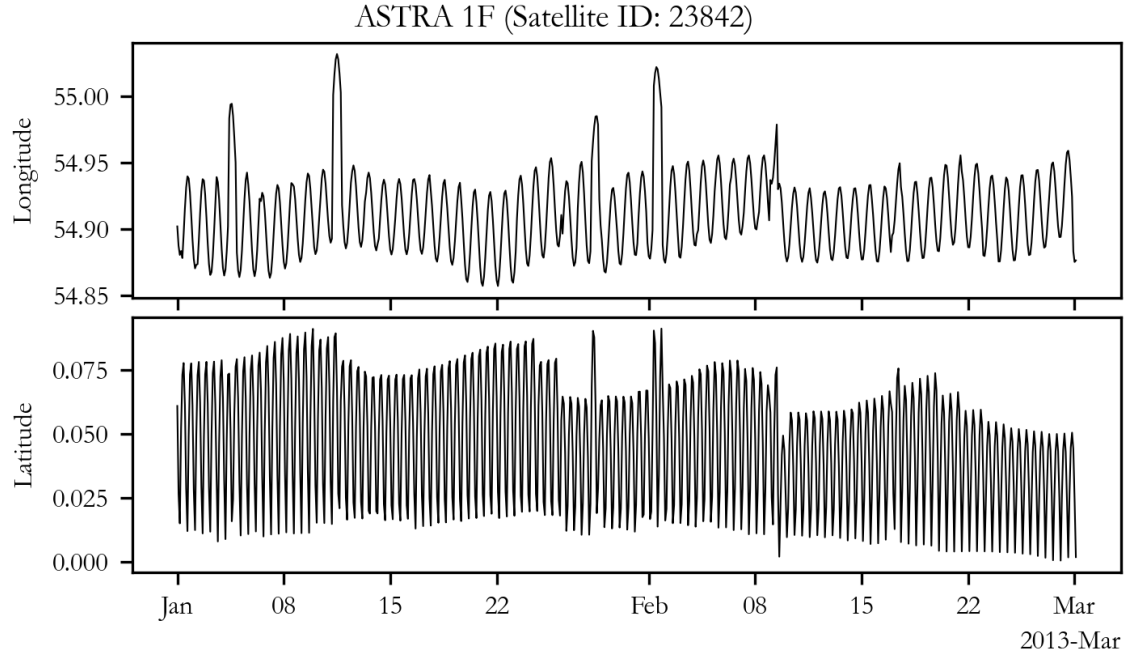

(b)

Figure 1-2: **Comparison of an electrically-propelled and chemically-propelled station-keeping in GEO.** (a) Time history for *Eutelsat 172B* (Satellite ID: 42741), a high-power satellite based on the *Eurostar-3000EOR* bus with an electric propulsion system [2]. For this station-keeping scheme, the longitudinal range is extremely small at only 0.04°. (b) Time history for *ASTRA 1F* (Satellite ID: 23842), an SES communications satellite based on the *HS-601* bus with a chemical propulsion system [9]. The longitudinal range for this station-keeping scheme is approximately 0.2°, much larger than the electric system's.

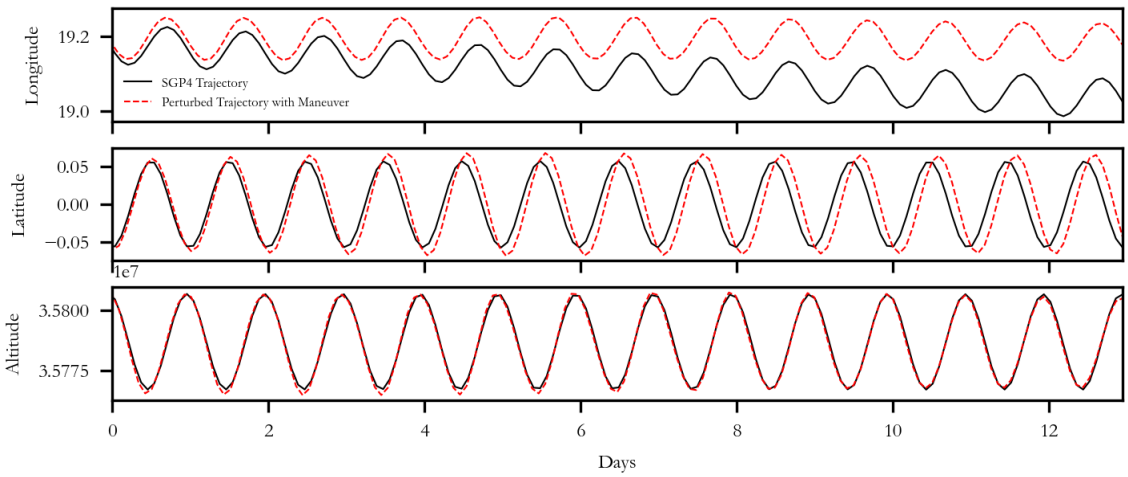

Figure 1-3: **Comparison of static and maneuver-aware trajectories.** The static trajectory (black) was propagated with SGP4 to simulate a stale, TLE-sourced orbit. The maneuver-aware trajectory (red) experienced a station-keeping maneuver at the beginning of the simulation window and was propagated with the MAPS propagator described in Chapter 3 which accounts for J2 perturbations as well as the gravitational effects of the Sun and Moon. This simulation shows that the two trajectories grow further apart with time. Determining the post-maneuver orbit becomes more difficult the longer the satellite's post-maneuver tracklets remain uncorrelated.

1-5 shows the angular and linear distance between three satellites in the ASTRA 19.2°E cluster over the span of 17 days. All three satellites operated within a 70 km station during this time, and sometimes two of these satellites passed less than 3 km from each other. Even under ideal conditions, it can be difficult for ground-based sensors to resolve objects that operate this closely. Non-ideal sensor location, weather patterns, and satellite orientation can make distinguishing between similarly clustered satellites nearly impossible. In cases like this, accounting for station-keeping maneuvers is essential to maintaining clean object histories.

1.2 Literature Review

1.2.1 PoL Usage and Applications

Despite the fact that the concept of PoL characterization has already been used to inform maneuver and anomalous behavior detection algorithms [30, 35, 63], the con-

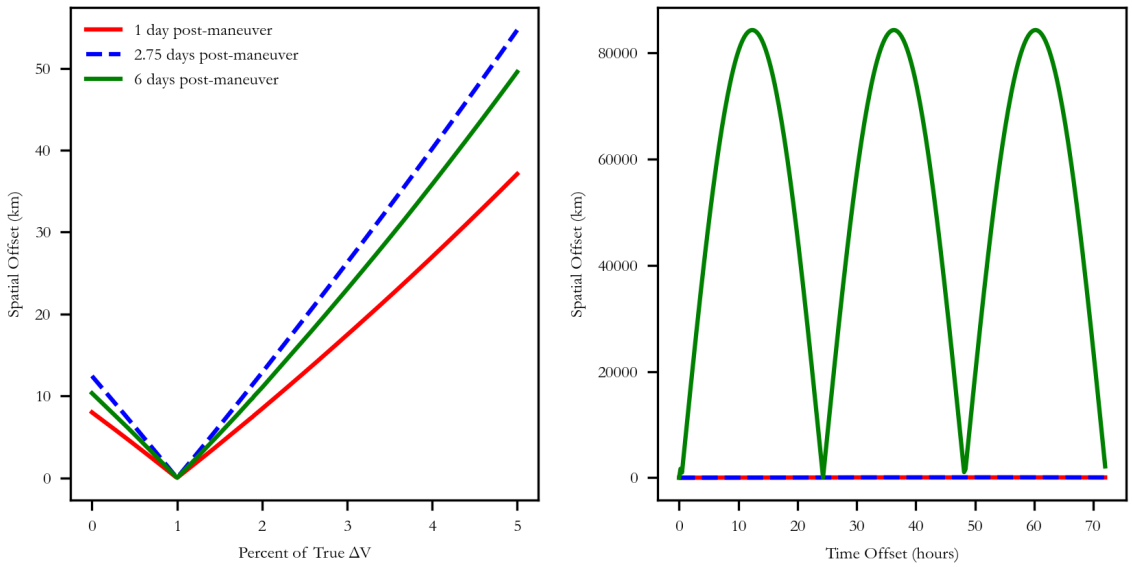

(a) (b)

Figure 1-4: **Error in propagated satellite position resulting from predicted maneuver time and ΔV errors.** (a) Error in kilometers for propagated satellite position as a function of error in predicted maneuver ΔV. This relationship is shown for three different observation times. (b) Error in kilometers for propagated satellite position as a function of error in predicted maneuver time. Again, this function is displayed for three inter-observation times. While the offset is linear for ΔV, it is parabolic and potentially much larger when resulting from maneuver time error.

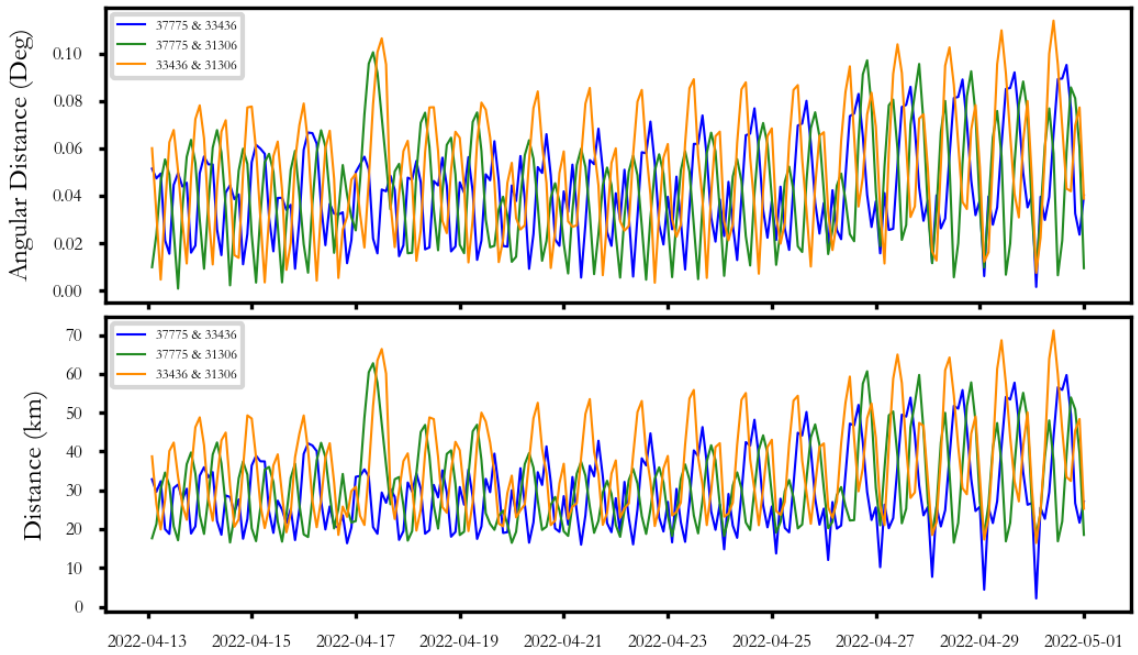

Figure 1-5: **Inter-satellite distances for three clustered GEO satellites.** Inter-satellite distances in degrees (top) and kilometers (bottom) for *ASTRA 1N* (Satellite ID: 37775), *ASTRA 1M* (Satellite ID: 33436), and *ASTRA 1L* (Satellite ID: 31306) in the SES-operated ASTRA 19.2°E satellite cluster. The maximum and minimum distances observed between *ASTRA 1N* and *ASTRA 1M* for this time period are 59.69 km and 2.13 km respectively which correspond to angular separations of 0.10048° and 0.00084°.

cept of PoL itself is nebulous within the research community. There is no standard for PoL characterization on which to base a communicable analysis between researchers and research objectives. In some works, the term *pattern of life* is used to refer to a sequence of historical data points, while in others it refers to the features of a distinct station-keeping routine or broader trends in maneuver behavior [19, 48, 16, 7]. This inconsistency requires that the structure of a PoL must be defined on a case-by-case basis depending on the target analysis, and these definitions are often difficult to generalize.

Describing PoLs as sequences of station-keeping objectives or timelines of individual maneuvers poses problems when applied to diverse groups of satellites and analysis objectives. Segmenting a satellite's PoL by station-keeping objective requires prior knowledge of the satellite's mission or of behaviors associated with the designated objectives; this information is not always readily accessible [22, 20]. Systems that characterize PoL via maneuver detection and characterization are complicated by the diversity of maneuver profiles in GEO. In addition to single-burn maneuvers, a maneuver-dependent PoL model would have to accommodate satellites that perform long burns or multiple, consecutive burns for the same objective. As a result, maneuver classification is highly subjective because many conventions must be adopted for how to characterize all of these maneuvers in a way that is useful to PoL analysis. Maneuver-dependent conventions also neglect passive behaviors, focusing on periods of activity instead of larger patterns in a satellite's life cycle. For these reasons, a generalized PoL model cannot be maneuver-dependent at the macro level.

1.2.2 Orbit Determination and Maneuver Prediction

PoL characterization at all levels is highly dependent on the time-density and format of the historical data being analyzed. The NORAD satellite catalogue is maintained by correlating optical or radar tracklets for pre-catalogued objects, but uncorrelated tracklets can accumulate when orbit information is inaccurate or outdated [22, 40, 65]. This can be the result of sparse observations, measurement noise, low ground-station availability, or degraded data [33, 21, 53, 31]. Frequent maneuvers make orbit de-

termination even more difficult, especially in the more crowded portions of the geostationary belt [44, 56]. Tracking in object-dense areas can be significantly impacted by the uncertainty introduced by sensing techniques, making multiple nearby objects difficult to resolve and resulting in cross-tagged satellite data [64, 28]. Cross-tagging and uncorrelated tracklets often happen during and after maneuvers since multiple post-maneuver tracklets are necessary to recover the orbit [60, 38, 41].

Maneuver prediction techniques can mitigate some of the challenging aspects of satellite tracking and orbit recovery. Shabarekh et al. [58, 57] developed a probabilistic Interval Similarity Model (ISM) that was able to correctly predict maneuvers for *Galaxy 15* (Satellite ID: 28884) at a resolution of 24-hour time steps during extended periods of regular station-keeping. Qin et al. demonstrated that services provided by the BeiDou Navigation Satellite System (BDS) can be improved by predicting and accounting for station-keeping maneuvers [46]. A few efforts are focused on predicting a satellite's post-maneuver state or its station-keeping control objectives as a means of maneuver prediction [59, 17]. These methods have been shown to be reasonably effective for individual satellites or station-keeping schemes. However, they have not been tested for large-scale satellite tracking, and currently, it is more common for analysts to employ generalized maneuver detection algorithms to characterize maneuver time and ΔV rather than use proactive prediction methods [45, 42, 66, 18].

1.3 Collaborative and Accessible SSA

Understanding satellite behavior and associated intent is an integral component of SSA, but there is very little accountability among operators to disclose detailed mission objectives and precise orbital data or to adhere to operational guidelines [20, 22]. The challenges posed by this lack of communication will escalate as more satellites are operated and abandoned in the already crowded geostationary belt [26, 61]. Persistent surveillance of both active payloads and debris is necessary to determine object trajectories and assess potential collision risks, but catalogue discrepancies and poor integration between data sources continue to interfere with satellite tracking and data analysis efforts [22, 61, 65]. Collaborative SSA can address many of these systemic problems by making data, software, and best practices more accessible to researchers, operators, and analysts. This includes improved communication and conformity of nomenclature, not just between operators, but between operators, analysts, and SSA software developers who may not have first-hand experience with operational challenges. This work presents two Python-based SSA tools designed to combat data accessibility and quality obstacles common to researchers and operators alike.

Chapter 2 proposes a nomenclature for a generalizable PoL model and, accordingly, presents a simple algorithm that can quickly characterize PoLs for a large number of satellite histories to identify instances of macro-level behavioral modes. The algorithm is able to isolate PoL shifts - called nodes - even from sparse or low-precision position histories like collections of two-line-element sets (TLE), meaning that it is effective regardless of the user's access to high-quality, proprietary orbital data. It is particularly efficient as a method of isolating training data for more complex analyses. For example, the tool can quickly locate periods of nominal station-keeping in hundreds of satellite histories so that this behavior can be analyzed by a clustering algorithm or another machine learning technique [20, 52].

Evaluating realistic confidence in the error associated with orbital estimates is another SSA challenge made more difficult by a communication disconnect. Errors in orbital data can be caused by imperfect propagation or measurements - the details

of which are not publicly released for many data sources [22]. Frequent undisclosed maneuvers also contribute to this error since tracklets observed during and directly after a maneuver are often uncorrelated or yield poor orbital estimates until the arc of active tracklets no longer includes pre-maneuver observations [44]. This is one reason why maneuver prediction, especially during periods of regular station-keeping, is so appealing. Unfortunately, many maneuver prediction models are designed around or exclusively tested on a single satellite or aggregated system and focus solely on the timing of predicted maneuvers [58, 45]. Time comparison results can provide an informative metric for a model's ability to recognize behavior abnormalities, especially when the context is singular. However, more information is necessary to determine whether a particular model can provide the precision and accuracy necessary to work with specific sensors, data, or software. Hence, when evaluating model performance for more general applications like catalogue hygiene, it is more helpful to characterize prediction results in terms of the satellite's post-maneuver location or state.

To that end, Chapter 3 presents a simulation tool that evaluates probabilistic maneuver prediction models in the context of physical viewing constraints. It allows users to define a prediction model and a surveillance scenario in which a satellite maneuvers in the time between two observations. Then it generates the spatial probability distribution for the satellite's predicted location at the post-maneuver observation time and plots it according to the viewing angles and constraints determined by the surveillance scenario. Chapter 4 discusses the potential impact and expansion of this tool and of the PoL characterization framework described in Chapter 2.

Chapter 2

SNICT: A tool for isolating Pattern of Life shifts in the Geosynchronous regime

Characterizing PoLs for a diverse range of Geosynchronous satellites is essential to contextualizing historic on-orbit behaviors and cultivating the capabilities to recognize and predict nominal and abnormal satellite behavior. On a general level, this analysis is preceded by processing extensive amounts of historical data in order to identify study periods relevant to a specific research objective. The Satellite Node Identification and Classification Tool - SNICT for short - provides a simple algorithmic approach to identifying shifts in behavioral modes and detecting PoL nodes from historical geographic positional data. Nodes are characterized by changes to the satellite's orbital station or drift and belong to one of three classes: "initiate drift" (ID), "end drift" (ED), and "adjust drift" (AD). Section 2.1 provides more detailed descriptions of each type of node and their relation to transitional and stationary behavioral modes. Section 2.2 explains how the SNICT algorithm was structured and tested on 18 satellite histories generated from two-line element (TLE) sets, and Section 2.3 discusses the results of these tests and highlights SNICT's performance when applied to several node-dense histories.

2.1 Pattern of Life Nodes and Behavioral Modes

A satellite's pattern of life has two fundamental components: nodes and behavioral modes. A node represents an instantaneous point on a PoL timeline between two behavioral modes and can be identified by inspecting historical positional data. A PoL node may occur at a time that a satellite has maneuvered, as is the case for longitudinal shift maneuvers. However, some nodes occur when no maneuver has been performed. For example, a satellite may cease North-South station-keeping near the end of its life-span or stop station-keeping altogether. These events would constitute a PoL shift, and a node would occur in the absence of a course-altering maneuver. For this reason, SNICT does not rely on maneuver detection or characterization. In fact, SNICT uses a very simple algorithm to identify nodes.

There are many types of events beyond end-of-life (EoL) behaviors that can comprise shifts in PoL, but at the macro level, the vast majority are identifiable from a satellite's geographic positional history [49]. In fact, orbit insertion, changes-in-station, and retirement maneuvers can all be extrapolated from geographic longitude without incurring additional complexity from inclined orbits or small variations in station-keeping cycles. For this reason, SNICT determines ID, ED, and AD nodes from longitudinal position histories like those shown in Figures 2-1 and 2-2.

The modes that fall between node pairs and can be broadly grouped into transitional modes — preceded by an ID or AD node — or stationary modes — preceded by an ED node. Stationary modes are periods within which a satellite performed regular station-keeping maneuvers, or in other words, its periodic motion was centered at a consistent longitudinal position and did not exceed a longitudinal amplitude larger than one orbital slot. Since the size of one orbital slot is not currently regulated, this work assumes a slot width of half of a longitudinal degree. ID nodes occur when a satellite that has previously been station-keeping at a consistent longitude leaves that station. They are preceded by a stationary mode and followed by a transitional mode, such as a longitudinal drift, a libration orbit, or a period of increased eccentricity. ED nodes follow transitional modes if the satellite has resumed station-keeping at a

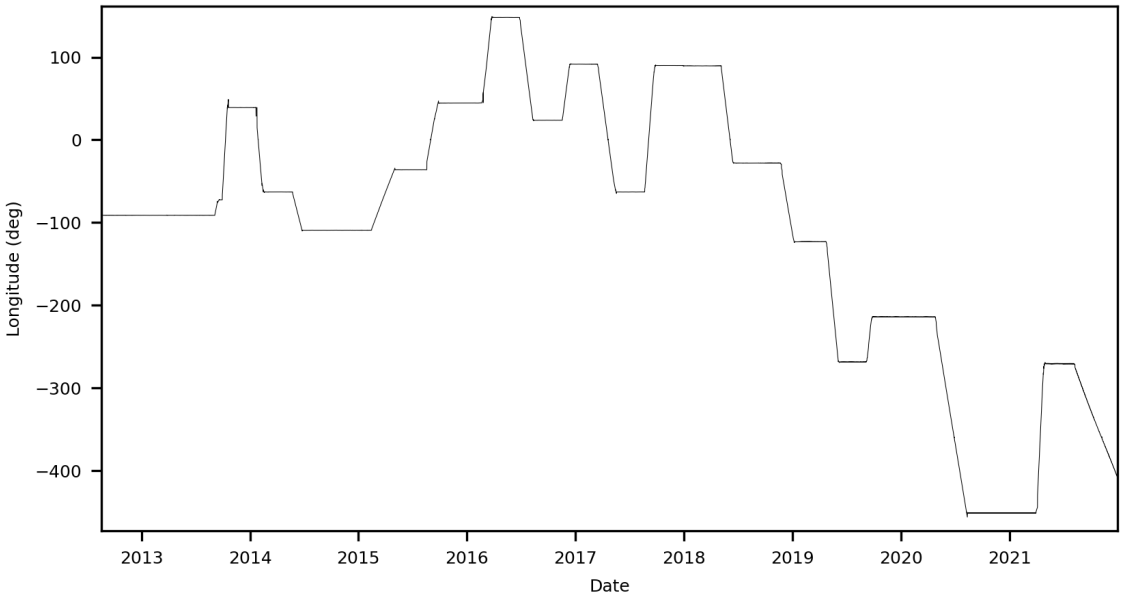

Figure 2-1: **Longitudinal position history for a GEO satellite.** Longitudinal position history for *NIMIQ-2* (Satellite ID: 27632).

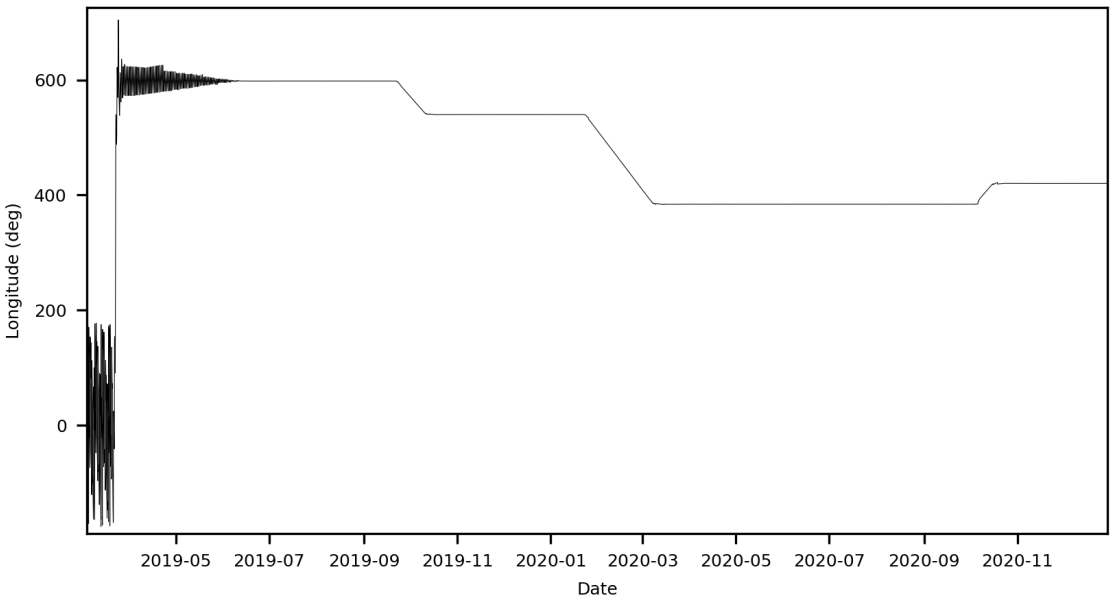

Figure 2-2: **Longitudinal position history for a GEO satellite.** Longitudinal position history for *WGS-10* (Satellite ID: 44071).

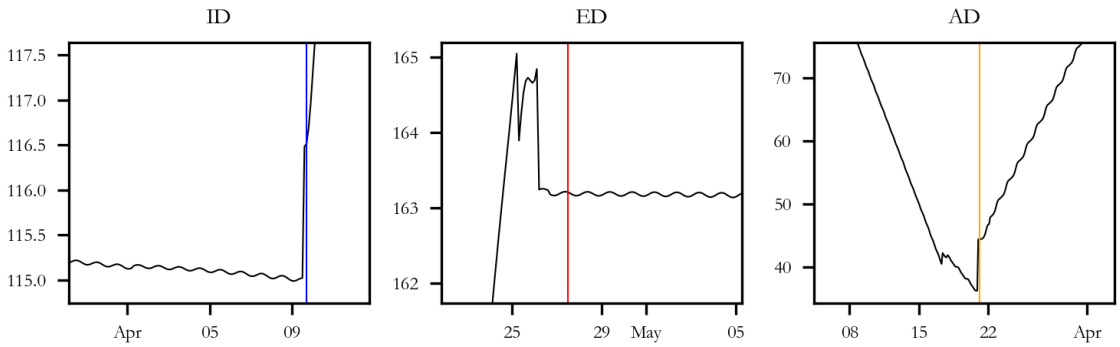

Figure 2-3: **Examples of ID, ED, and AD nodes.** Examples of ID (blue), ED (red), and AD (orange) node detections from the longitudinal position history of *SHIJIAN-17* (Satellite ID: 41838).

consistent longitude. AD nodes capture behavioral changes that occur between two transitional modes. For example, an AD node would be detected if a satellite's drift rate or direction changed suddenly during a longitudinal shift maneuver or if there was a sudden change in trajectory during orbit insertion. This allows for more than one distinct behavioral mode between an ID and an ED node pair and is particularly important when characterizing PoL for satellites with non-circular orbits that do not satisfy the criteria for stationary modes.

2.2 Methodology

2.2.1 Algorithm Inputs

The longitude waveforms applied to the SNICT algorithm were generated from historical two-line elements (TLEs) provided by the United States Space Force's 18th Space Control Squadron (18 SpCS) and accessed via Space-Track.org. As demonstrated in Figure 2-4, TLE-generated data is often noisy due to cross-tagging, outdated orbit-determination methods, and inconsistent observation schedules, but this source was chosen in order to demonstrate the PoL characterization system described in Section 1.1.1 on a publicly available source of historical orbital data. However, since SNICT and this PoL system are only directly dependent on geographic positional data, they can be used with other data sources, orbit determination methods, and propagation

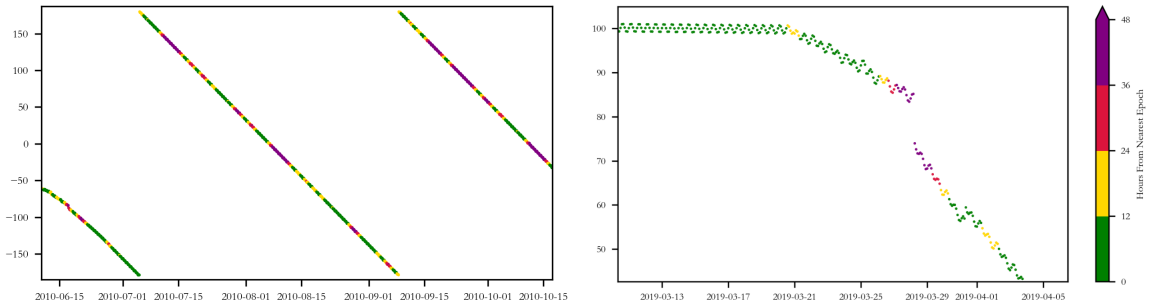

Figure 2-4: **Example of Longitude Data Generated from TLEs.** Example of Longitude Data Generated from TLEs provided by the United States Space Force's 18th Space Control Squadron for *TDRS-1* (Satellite ID: 13969) (left) and *FLTSATCOM-7* (Satellite ID: 17181) (right). Data points are color-coded to indicate the timestamp's distance in hours from the nearest TLE epoch. There are gaps and large jumps in the longitude histories due to anomalies in the TLE source data.

models as long as the inputs are properly interpolated.

To account for anomalies in the source data, ID and ED nodes were discarded for longitude displacements with durations of less than 24 hours. That is, if a potential transition was detected but the satellite resumed its pre-detection longitude less than 24 hours after the detection, the transition was assumed to be the result of a source data anomaly. Longitudes were taken from ephemerides converted from the TLE source data for a study period spanning January 1st, 2010 to December 31st, 2021 [51, 34, 3]. The ephemerides were generated at a timestep of two hours in order to sufficiently capture the longitude sinusoid observed over the course of one orbital period.

2.2.2 Node Detection and Filtering

SNICT requires two inputs: an array of sequential longitudes and an array of their corresponding timestamps. The standard deviation of the longitude is processed in increments equivalent to one orbital period, starting with the first 24 hours for geosynchronous orbits, then shifting this 24-hour window forward by one timestep at a time as shown in Figure 2-5. The standard deviation calculated for each window is associated with the last timestamp within that window so that each timestamp corresponds to a value of longitude and the standard deviation of the longitude signal

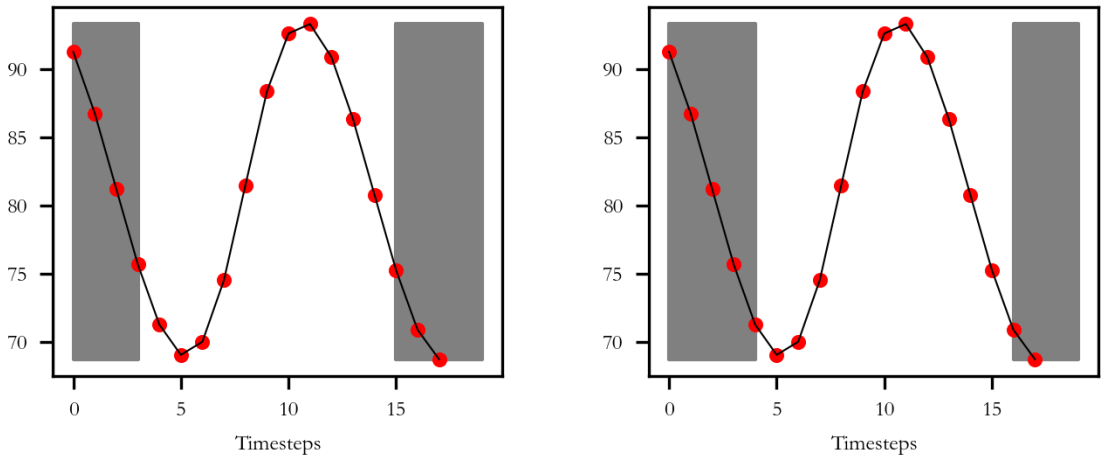

Figure 2-5: **Window of longitudinal position history used to calculate the standard deviation.** The standard deviation is calculated from all data points within the window (set against the white background). In the first pane, the calculated value is associated with step 15. The next step is shown in the second pane, after which the calculated standard deviation is associated with step 16.

over the previous 24 hours. Every timestamp within the first 24 hours is assigned one standard deviation value which is taken across this time frame since the calculation cannot span an entire orbital period until the first data point is at least 24 hours behind the last timestamp in the current window.

SNICT then steps through each timestamp within the study period, looking for a standard deviation that is greater than the stationary mode threshold — set to a value of 0.03 for this study. When found, the timestamp and its meta-data are archived as a potential ID node, and a flag is set to indicate that the satellite has entered a transitional mode. As the algorithm continues to step through timestamps, it can respond in either of two ways:

Case 1: If the standard deviation has fallen below the stationary threshold, SNICT must confirm that the satellite is actually in a new stationary mode. It does this by confirming that the satellite's longitude over the next orbital period does not fluctuate more than three-tenths of a degree. If this is confirmed, the current timestamp and its meta-data are archived as a potential ED node, the flag indicating a transitional mode is toggled off, and the algorithm resumes checking the standard deviation at each timestamp for a potential ID node. If the new mode is not confirmed, the

	SME Analysis	Detections	Correlated Detections	Fraction Correlated
ID	125	113	106	0.848
ED	130	111	109	0.838
AD	189	393	154	0.815
Total	444	617	369	0.831

Table 2.1: **Comparison of SME Node Analysis and Algorithmic Node Detection.** Correlated detections are nodes that correspond to specific SME nodes.

algorithm moves on to Case 2.

Case 2: If the standard deviation has risen by more than 110% since the last timestep, the current timestamp and its meta-data are archived as a potential AD node. The algorithm then continues stepping through each timestamp checking for Case 1 or Case 2.

Once the entire satellite history has been processed, SNICT filters the potential nodes for redundant detections. This includes ID nodes that follow ED nodes by less than 48 hours and AD nodes that fall within 24 hours of each other. Any ED-ID node pairs that are filtered out at this stage are replaced by AD nodes, and strings of redundant AD nodes default to the first detection in the string. Once a potential detection is confirmed, a node is created from the satellite's NORAD catalog number, the detection timestamp, the two-character node type designator, and other optional meta-data. SNICT was applied to a group of 18 GEO satellites, and the detected nodes were compared to a database of PoL nodes manually labeled by a subject matter expert (SME) [3].

2.3 Results

SNICT was demonstrated on the historical longitudinal positional data of 18 satellites within the study period. This group included satellites from eight different countries utilizing various chemical, electric, and hybrid propulsion systems and representing numerous missions including meteorological, communication, and military objectives.

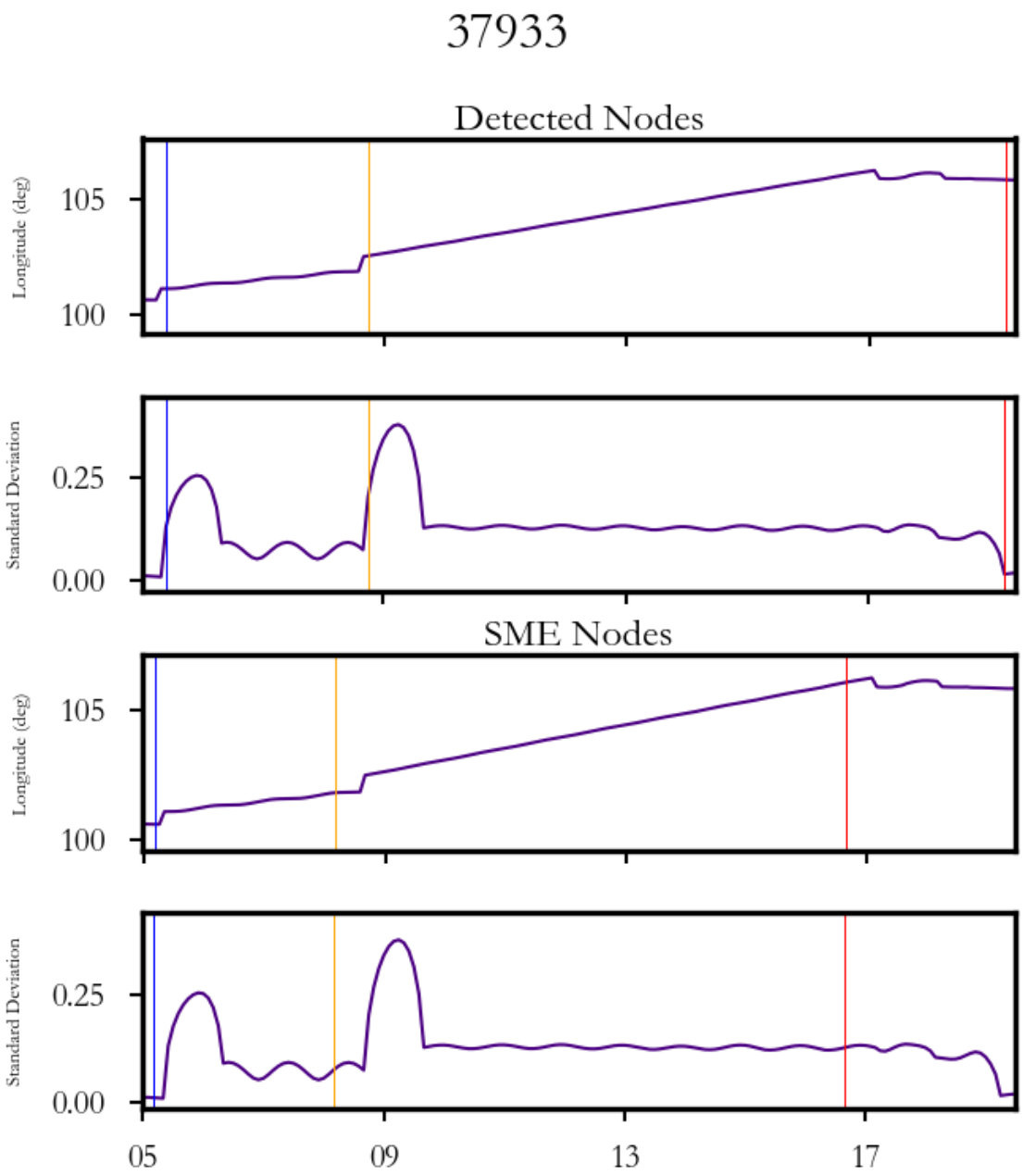

Figure 2-6: **Example of correlated ID, AD, and ED nodes.** In this segment of the longitudinal position history for *ASIASAT-7* (Satellite ID: 37933), the ID (blue), AD (orange), and ED (Red) node detections in the first pane are correlated with the ID, AD, and ED nodes in the third pane that were recorded during a SME analysis. The second and fourth rows show the standard deviation during these detections.

According to the SME analysis, there are a combined 444 nodes in these 18 histories. SNICT detected 617, and 369 of those detections were correlated with the SME nodes, meaning that they shared the same node designation and were timestamped near the same TLE epoch. Figure 2-6 shows a detection window with three correlated nodes, one of each node designation.

Many of the uncorrelated detections were timestamped with the same epoch as SME nodes but had a different designation. For example, some of the nodes typed as ID and ED in the SME dataset were captured as AD nodes by SNICT. The opposite also occurred, where the algorithm segmented longer transitional modes from the SME into smaller sections with additional ED and ID nodes. SNICT seemed to struggle the most with placing ED nodes when the standard deviation in stationary modes remained relatively high, as is the case for the satellite history in Figure 2-7.

Despite these inconsistencies in the AD node detections, SNICT was largely successful at partitioning transitional modes across node-dense longitude histories. The histories for *NIMIQ-2* (27632), *HYLAS-1* (37237), and *Luch / Olymp-K* (40258) contained the highest number of SME nodes.

As shown in Figure 2-8, there were some missing and uncorrelated AD node detections for *NIMIQ-2*. However, every ID and ED node was correlated. There are several AD nodes that follow ID nodes so closely that the ID nodes are difficult to distinguish in the plot, but SNICT detected ID and ED nodes within a few hours of all of the SME nodes of those designations. The results presented in Figure 2-9 for *HYLAS-1* were similar. After orbit insertion, there were seven uncorrelated AD node detections and one uncorrelated SME-generated AD node. All of the remaining nodes were correlated. The number of AD detections for *Luch / Olymp-K* in Figure 2-10 were noticeably less than *NIMIQ-2* and *HYLAS-1* with only 32 detections compared to the 42 recorded by the SME. All other nodes were correlated except the first ED and ID nodes which SNICT designated as AD nodes due to the short stationary mode between them.

In most cases, SNICT detected significantly more AD nodes than were recorded by the SME. This outcome is not surprising since AD detections were not filtered to

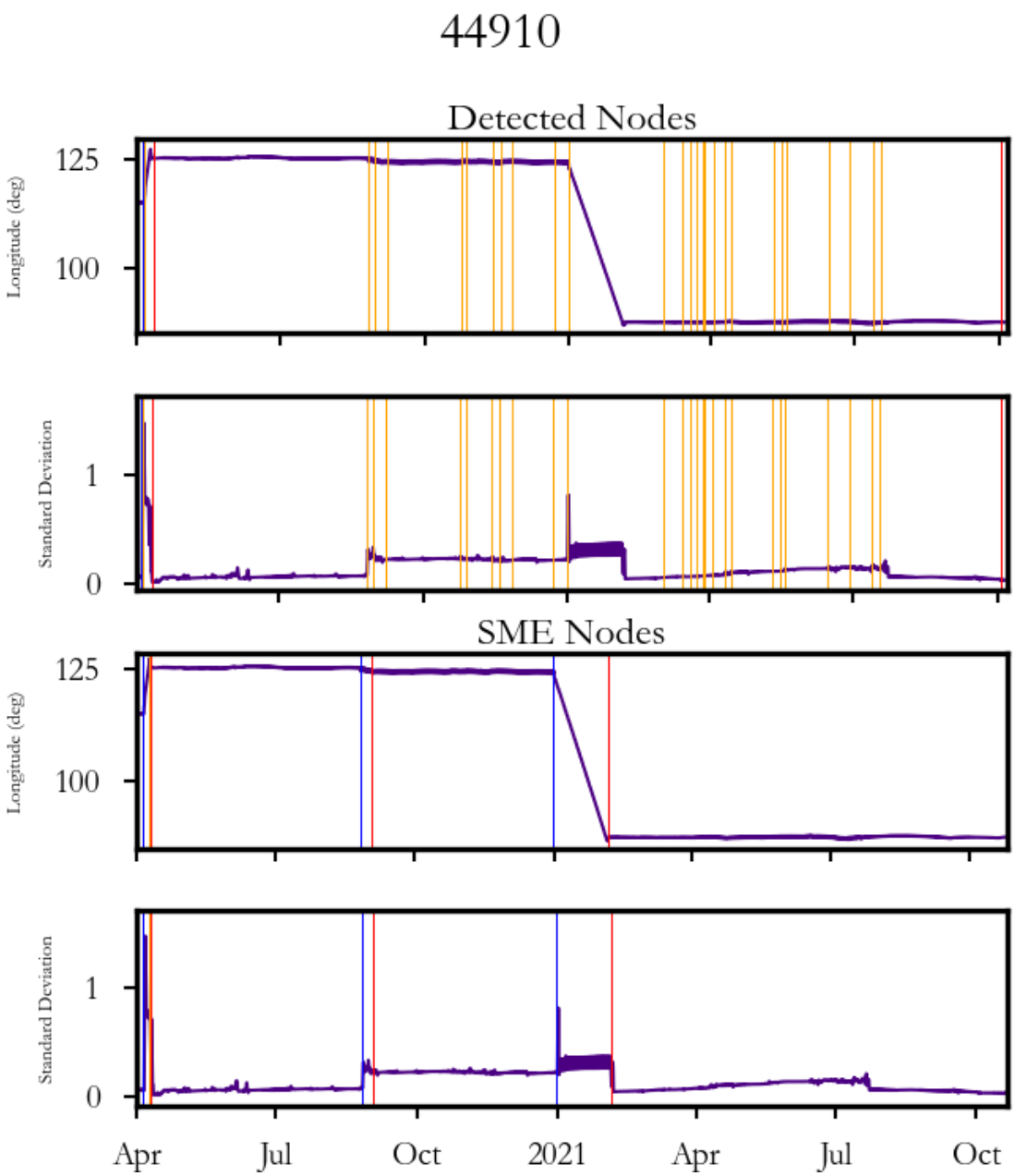

Figure 2-7: **Example of ID and ED nodes detected as AD nodes.** Example of ED nodes (red) detected as AD nodes (orange) in longitudinal position history for *SJ-20* (Satellite ID: 44910). There are many uncorrelated AD node detections in the first two panes. Some of these correspond to the four uncorrelated SME nodes in the bottom two panes.

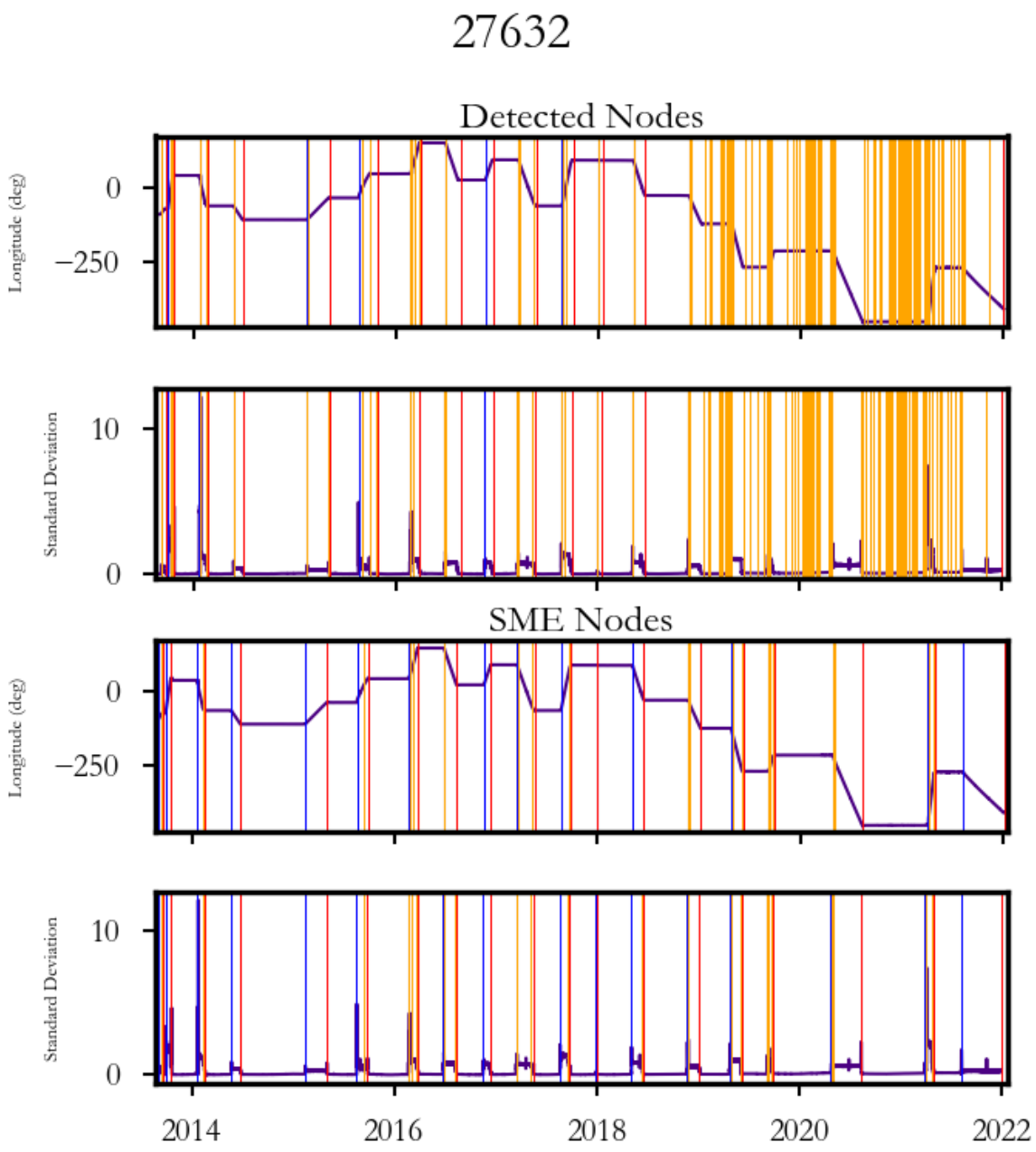

Figure 2-8: **Comparison of SNICT and SME Analysis Results for *NIMIQ-2* (Satellite ID: 27632).**

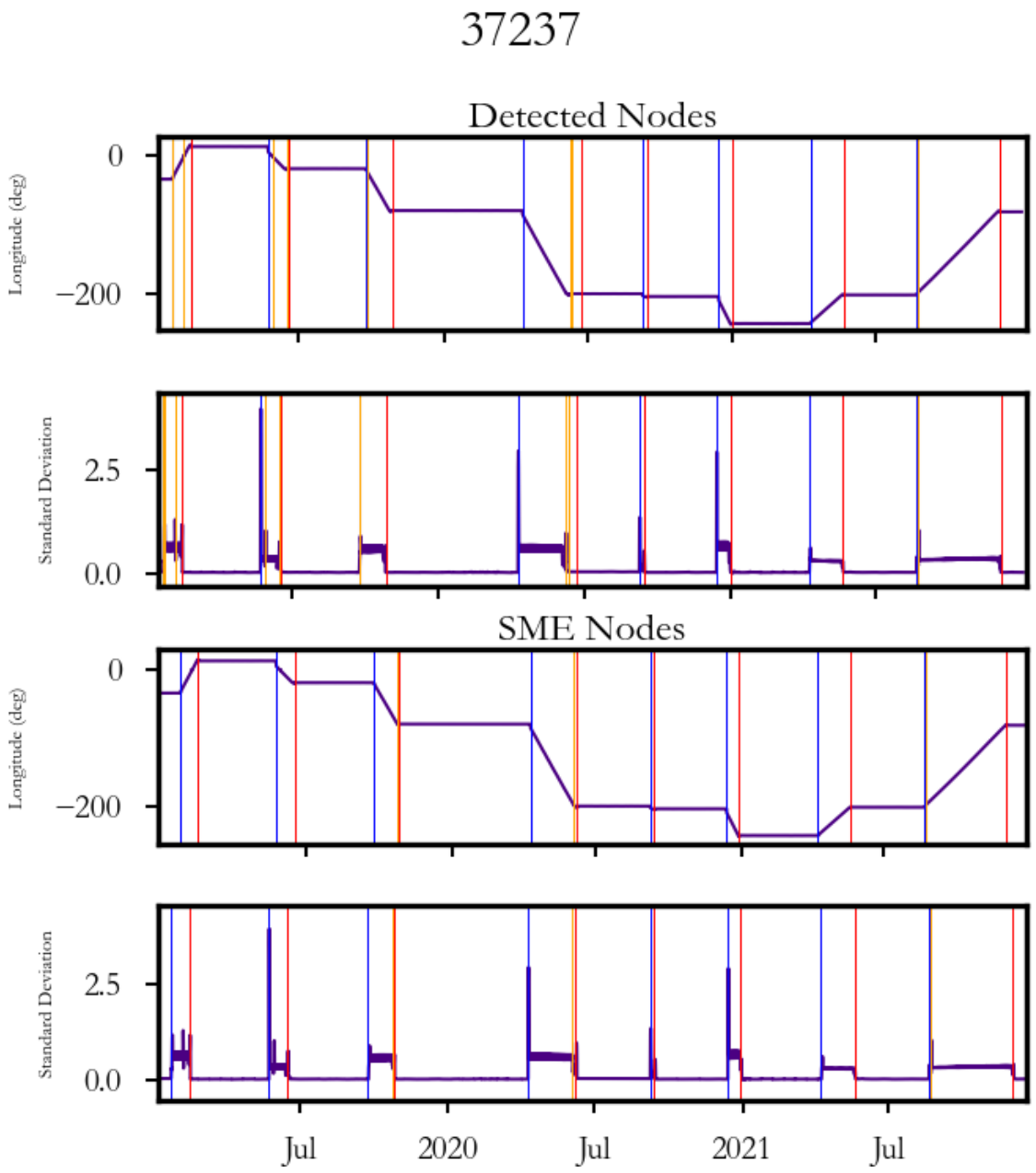

Figure 2-9: **Comparison of SNICT and SME Analysis Results for *HYLAS-1* (Satellite ID: 37237).**

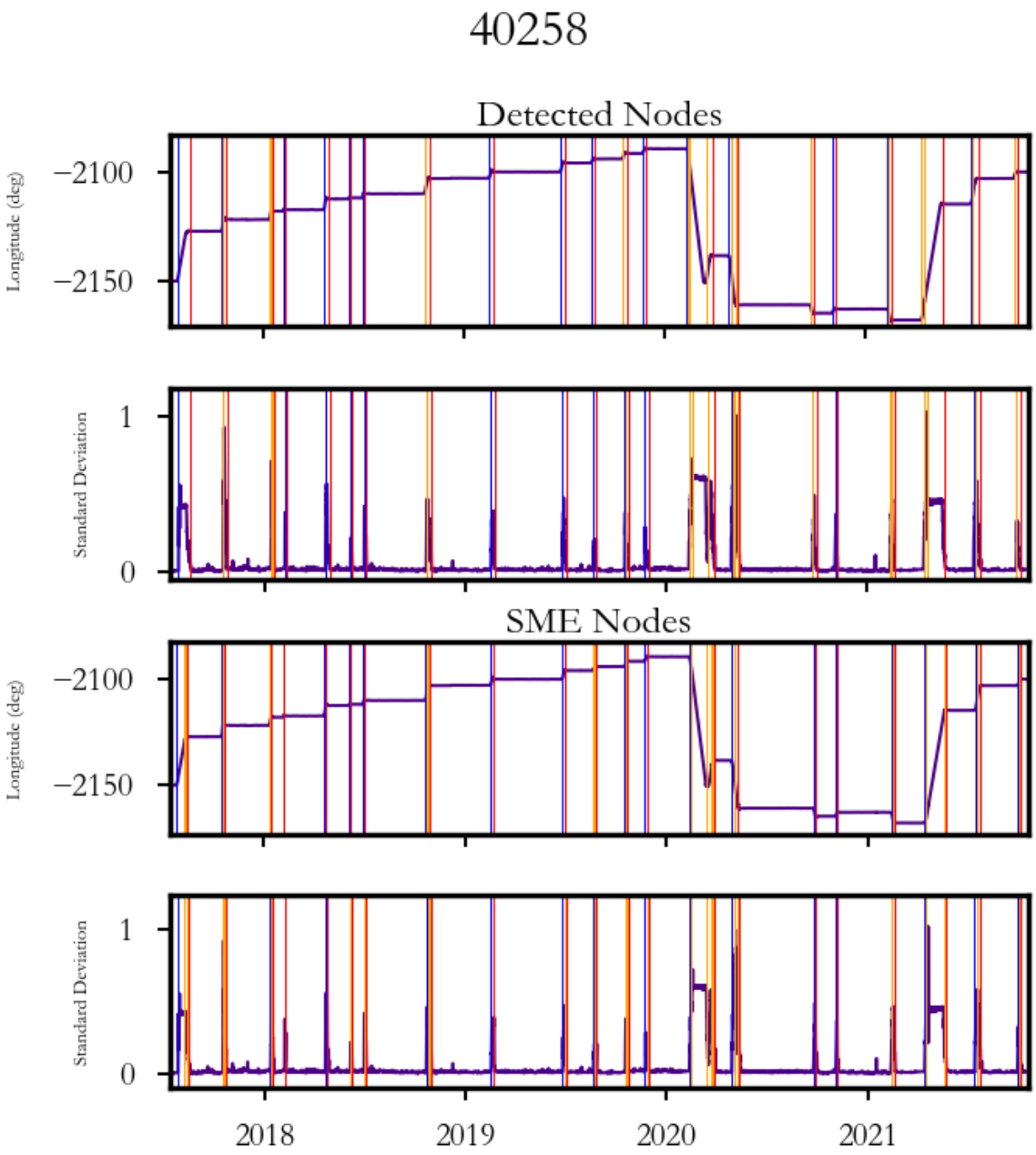

Figure 2-10: **Comparison of SNICT and SME Analysis Results for *Luch / Olymp-K* (Satellite ID: 40258).**

exclude anomalies in the TLE source data while these anomalies were often visually identifiable and therefore unlabelled during the SME analysis. Additionally, some of the nodes designated as ID and ED by the SME analysis were captured by SNICT as AD nodes due to factors such as the algorithm's higher time resolution and the aforementioned lack of AD filtering - which particularly influenced ED node designations. Based on these results, increased source data resolution and accuracy would likely produce better results by reducing the number of anomalies and extraneous node detections. However, more than 83% of all SME nodes were directly correlated with detections, and the histories with the highest node densities detected 89% or more. These correlation fractions are quite high considering the low resolution and precision of the input data in the context of SNICT's simplistic detection algorithm.

In combination with reducing false detections and cross-designated nodes via higher-quality orbital data, SNICT would benefit from a dynamic detection threshold, especially for identifying ED nodes. This might be accomplished through machine learning techniques or additional analysis of standard deviation signals. Further study of transitional mode end-points will be necessary to gauge the applicability of such methods. To that end, it would be beneficial to establish explicit guidelines for ED node placement between transitional and stationary modes so that periods of consistent station-keeping behavior may be reliably isolated for independent study. SNICT could conceivably be used to quickly parse large satellite histories to identify training data for prediction models, but its utility is hampered when stationary mode boundaries are inflated to include behavioral outliers as this can lead to poor estimates of optimal maneuver times and ΔV. Chapter 3 addresses the effects such uncertainties have on satellite tracking and describes a tool designed to simulate their impact under various constraints.

Chapter 3

MAPS: A tool for contextualizing and evaluating predicted maneuver models

GEO satellites are subject to perturbations such as non-uniform gravitational effects and solar radiation pressure that require them to maneuver frequently in order to maintain consistent Earth-relative stations. As discussed in Chapter 1, GEO satellites have many station-keeping schemes with different frequencies, magnitudes, and combinations of maneuver objectives. Even individual satellites, between one station-keeping cycle and the next, may display small changes in the frequency, magnitude, and direction of their maneuvers without entering into a new behavioral mode. This diversity of maneuver routines makes generalized maneuver prediction quite difficult since techniques that perform well for one satellite may perform poorly for many others. This chapter describes the Maneuver-Aware Probabilistic Simulator (MAPS), a tool designed to help operators, researchers, and analysts evaluate the efficacy of maneuver prediction models in context of satellite tracking. Section 3.1 discusses MAPS's framework for specifying satellite positions, and Section 3.2 details its code structure and data flow. Finally, in Section 3.3, the tool's capabilities are demonstrated on three generic prediction models applied to a GEO satellite operating in a close-proximity cluster.

3.1 Defining Satellite Coordinates

MAPS creates probability distributions of a satellite's post-maneuver position by repeatedly propagating its orbit from an initial state to a future observation time while varying the maneuver parameters. A key component of this analysis involves knowing the satellite's true location at the observation time, but these coordinates cannot be directly defined by the user. Instead, MAPS determines the true location by propagating the orbit from the initial state and the set of true maneuver parameters. This is necessary due to the possibility of perturbation model discrepancies between MAPS and an external data source. Figure 3-1 shows three satellite trajectories propagated using different perturbation models from the same initial state. After five days, the position propagated with the Keplerian perturbation model deviates from the MAPS propagator by approximately 65 km which corresponds to an angular separation of more than one-tenth of a degree. As discussed in Chapter 1, these values exceed the maximum operational distance between satellites in tight clusters like ASTRA 19.2°E. Using a true location provided by an external propagator may introduce an offset comparable to the Keplerian model results or no offset at all, but for consistency, MAPS compares sampled satellite coordinates to an internally-propagated true location.

MAPS accepts coordinates in different reference frames depending on the target function. When a three-dimensional reference frame is needed, coordinates are either defined according to the Geocentric Celestial Reference System (GCRS) or the International Terrestrial Reference System (ITRS). Both systems are Earth-centered, but only ITRS is Earth-fixed [25]. GCRS is derived from the Barycentric Celestial Reference System (BCRS) and does not rotate with respect to extragalactic objects [29]. Since it is supported by most Python astronomy packages, MAPS uses GCRS as its propagation frame and, in some cases, to define the initial state vector. As an Earth-centered, Earth-fixed (ECEF) reference system, ITRS is useful for defining locations on or relative to the Earth's surface. The spherical representation of this frame consists of geodetic latitude, longitude, and altitude where altitude is measured

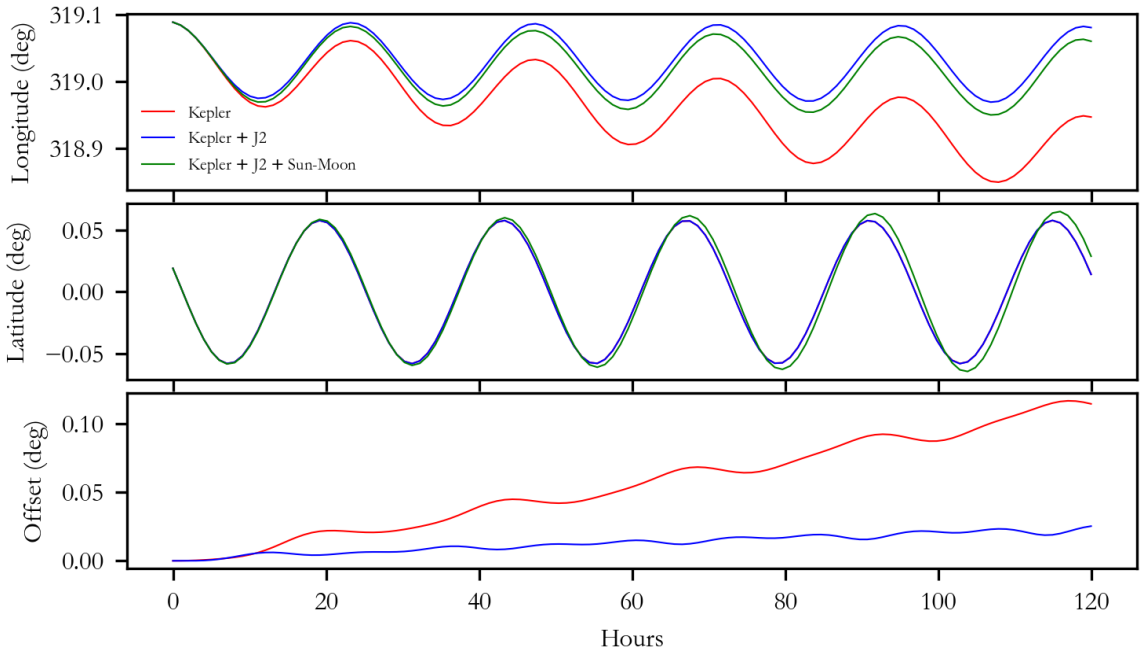

Figure 3-1: **Comparison of three perturbation models.** MAPS's perturbation model accounts for Keplerian accelerations, the J2 perturbation, and the gravitational effects of the Sun and Moon. The top two subplots include a GEO satellite's geodetic (ECEF) longitude (top) and latitude (middle) as derived by MAPS (green) a simple Keplerian model (red) and SGP4 (blue). The bottom subplot shows the angular offset of the Keplerian and SGP4 trajectories relative to the one generated by MAPS.

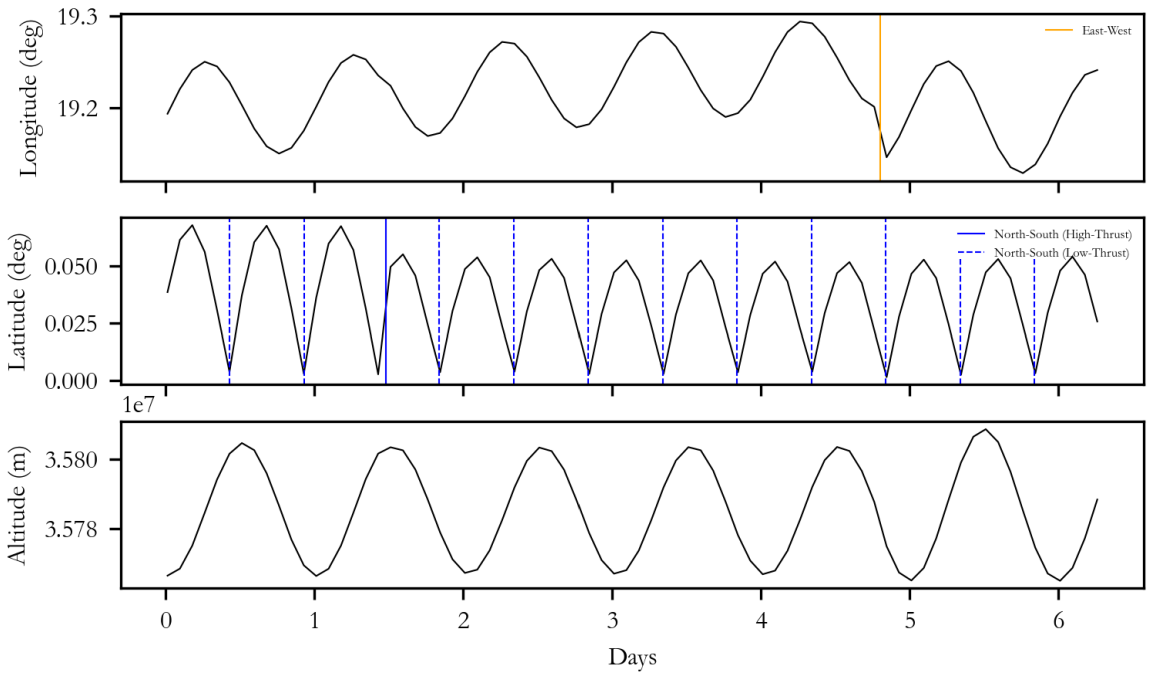

Figure 3-2: **Station-keeping maneuvers in a geographic positional history.** Historic ITRS-formatted positional data derived from TLEs for *ASTRA 1N* (Satellite ID: 37775). One East-West maneuver (orange) is marked in the longitudinal position history, and several North-South maneuvers (blue) are visible in the latitudinal position history. The North-South maneuver marked by a solid blue line represents a high-thrust chemical burn, and each dotted blue line indicates a low-thrust Hall-effect thruster burn [62].

as the distance above sea level. For geostationary satellites that station-keep within a small region of ground-relative space, ITRS coordinates can also reveal maneuver objectives. As shown in Figure 3-2, both East-West and North-South station-keeping are visible and distinguishable in ITRS latitude and longitude element histories.

Understanding a satellite's position in three dimensions is quite important when determining and propagating orbits, but some MAPS functions require a two-dimensional coordinate system. Three-dimensional views do not account for the constraints involved with satellite tracking, especially those introduced by ground-based observation. Ground-based sensors map satellite positions using only two parameters - their elevation angle and azimuth angle. A satellite's distance from a sensor cannot be determined from a single observation, so plotting position on a two-dimensional elevation-azimuth projection is more representative of a sensor's view of its target. As

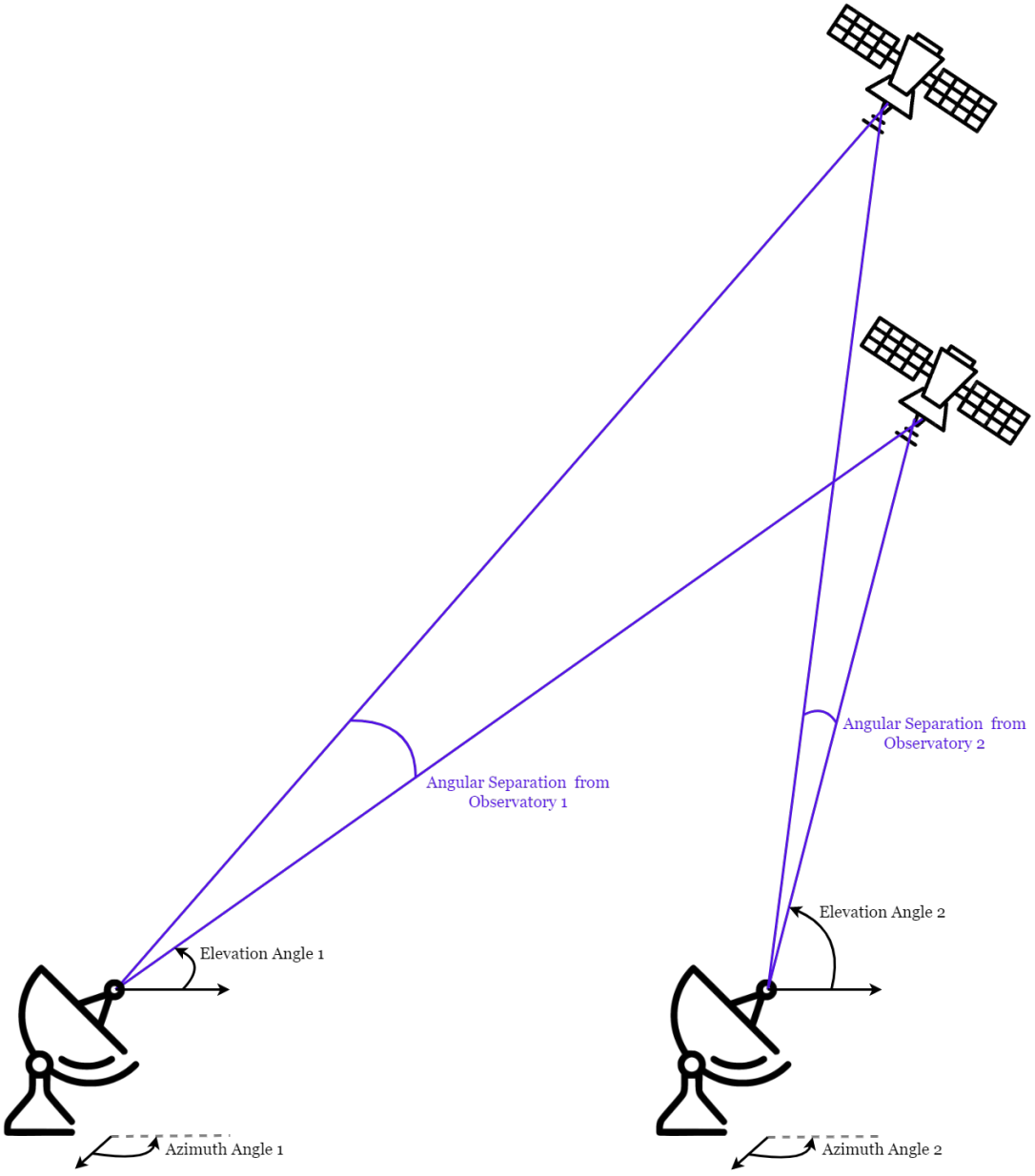

Figure 3-3: **Diagram of two ground-based sensor views.** Observatory 1 and Observatory 2 use different elevation, azimuth, and separation angles for the same satellites.

shown in Figure 3-3, a satellite's elevation and azimuth angles are measured from a specific location instead of in an Earth-centered reference frame. Notably, the angular distance between objects can vary drastically depending on the sensor location, so defining the observation point is crucial to understanding whether or not a satellite is actually resolvable from other nearby objects. If the distance between two satellites is small enough, their two probability distributions can overlap, increasing the risk for cross-tagging, and if their angular separation is smaller than the angular resolution of the sensor, then they will appear to be one object. Furthermore, if the probability distribution of a single satellite extends far beyond or is centered far outside of the sensor's field-of-view (FOV), then the prediction model may not be effective for that specific sensor or satellite. Therefore, the sensor location, resolution, and field-of-view (FOV) must be known to determine if a prediction model can realistically meet the accuracy and precision requirements imposed by observation constraints.

To that end, MAPS generates probability distributions that account for the FOV of ground-based observers. It can also incorporate information about other nearby objects, such as clustered satellites, and sensor resolution to provide realistic limitations on resolvable positions. This design allows users to test prediction models on combinations of maneuvers and constraints to evaluate whether the model is likely to be efficient for a specific use case.

3.2 MAPS Capabilities and Components

When provided with a satellite's last observed state and a maneuver prediction, MAPS uses Monte Carlo sampling, a `poliastro` propagation framework, and `Astropy` reference frame transformations to generate a probability distribution function (PDF) for the satellite's coordinates at a specified, post-maneuver observation time [6, 4, 5]. Figure 3-4 shows a simplified diagram of this process, the components of which are explained in more detail in this Section. Sections 3.2.1, 3.2.2, and 3.2.3 describe the format of each MAPS input, the propagation method, and the available output formats respectively.

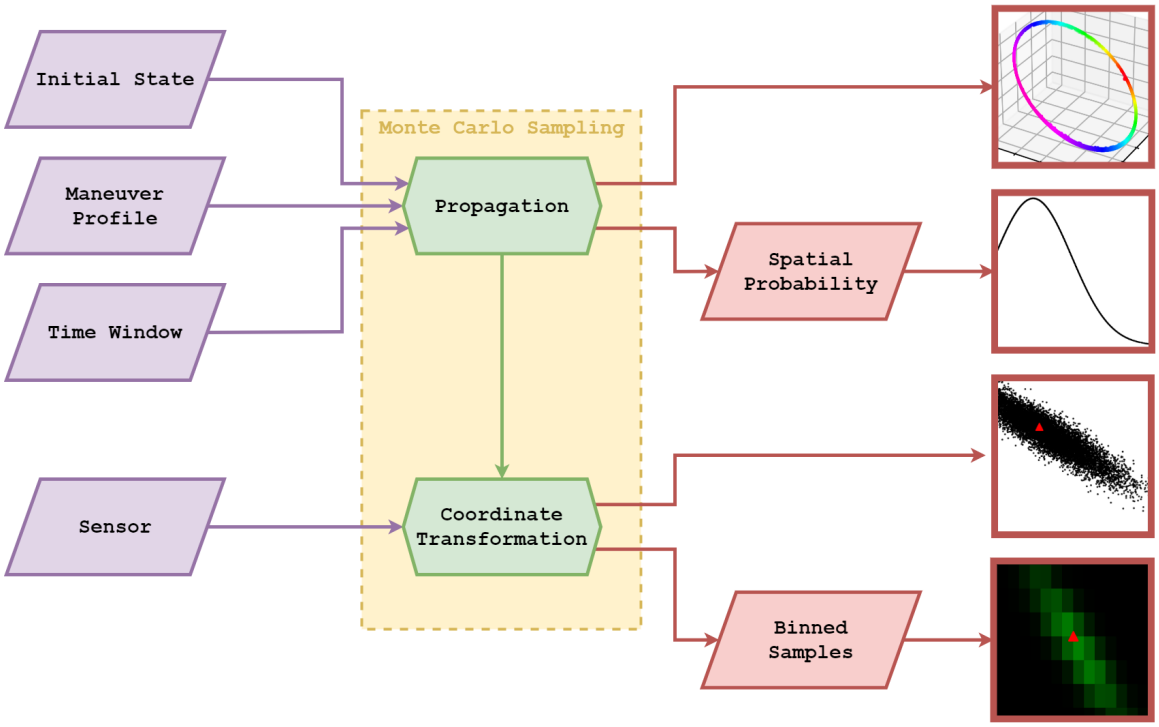

Figure 3-4: **Diagram of MAPS processes.** Diagram of MAPS inputs (purple), processes (green), and outputs (red).

3.2.1 MAPS Inputs

MAPS requires four inputs: the satellite's initial state, the simulation run time, a maneuver profile, and the number of simulations to be run. Some of these inputs have multiple components and must be instantiated as objects of specific MAPS classes to ensure they are correctly formatted.

Formatting Time Inputs

MAPS relies on the `datetime` module and `astropy.time` module to handle timestamps but does not require users to interact with these directly. Instead, all time inputs are formatted as strings or floating point numbers. The timestamp for the pre-maneuver observation - the start time - may be given as an ISO-formatted string [24]. MAPS converts this to an offset-aware `datetime` object and assumes the timestamp to be in the UTC timezone. The user must therefore take care to account for the timezone of the timestamp they provide and ensure it is converted to UTC time

if necessary. The remaining time inputs are more simply defined by floating point numbers corresponding to the number of seconds an event occurs after the start time. The run time provides MAPS with the time of the post-maneuver observation. It is the length of time that MAPS will propagate the satellite's position. The time components of the true and predicted maneuver models share this format as well.

Defining the Initial State

MAPS currently accepts the satellite's initial state as a set of orbital elements, as a TLE, or as position and velocity vectors. Since each of these inputs has several components, the initial state should be instantiated according to the type of input as an `OE`, `TLE`, or `RV` class object to ensure that MAPS receives the information in a consistent format. Instantiating `OE` objects requires arguments for the start time, the `astropy` distance unit associated with the given value of the semi-major axis, the `astropy` angle unit associated with the angular orbital elements, and a list of floating point values containing the orbital parameters. This list must have the order: semi-major axis, eccentricity, inclination, right ascension of the ascending node, argument of perigee, and true anomaly. The arguments for instantiating a `TLE` object are two strings corresponding to the first and second lines of the satellite's TLE. This class does not require an explicitly defined start time like the other two state classes, but it does require that the two input strings begin with the line number followed by a space. To generate an initial state from position and velocity vectors, the positions and velocities should be given as two lists and represented in Cartesian coordinates in the GCRS reference frame. Following the position and velocity lists, the remaining arguments for instantiating an `RV` object are the start time and the `astropy` distance unit corresponding to the given state vectors.

Maneuver Profiles

Maneuver profiles are combinations of true and predicted maneuver information. MAPS uses a single maneuver profile input that is formatted as a `maneuver_profile` class with attributes including the true maneuver parameters and their correspond-

ing probability distributions as defined by a prediction model. The class object must first be initialized with the true maneuver parameters before the predicted maneuver model can be incorporated with a particular class method.

The true maneuver parameters include the time that the maneuver occurred and the ΔV the satellite experienced during the maneuver. The ΔV is represented by three floating point numbers corresponding to the change in velocity in the x, y, and z directions in the GCRS reference frame. The user may specify whether these values are in units of meters per second or kilometers per second by providing the appropriate `astropy` distance unit when the maneuver model is initialized. Thus, the inputs for instantiating a `maneuver_profile` object are the true maneuver time, the x, y, and z components of ΔV, and, optionally, the unit of distance. If the unit is not specified, MAPS assumes it to be meters. Regardless of the distance unit, all velocities should be specified as a distance per second.

The predicted maneuver model encapsulates two lists of four floating point numbers. These define the probability distributions generated by a prediction model. In order, the four elements of each list correspond to the maneuver time, the x component of ΔV, the y component of ΔV, and the z component of ΔV. MAPS currently supports Gaussian probability distributions, so the first list includes the mean value of each parameter's distribution, and the second holds the corresponding standard deviations. These components must be added to the maneuver model using the class method associated with the distribution type. In this case, the method is `gaussian`, and the arguments are the list of means and the list of standard deviations. When the predicted maneuver model is incorporated into the model, the probability distribution for each parameter is generated via the `random` module so that it can be sampled randomly using a class method such as `time` or `dx`.

3.2.2 Orbit Propagation

MAPS propagates the satellite's orbit using a propagator from the `poliastro` python module [11]. Specifically, it uses a numerical propagator based on Cowell's formulation [27] in which the Keplerian acceleration can be separated from the perturbation

accelerations, a_p, as seen in Eq. 3.1.

$$\ddot{r} = -\frac{\mu}{|r|^3} r + a_p \tag{3.1}$$

The `poliastro` Cowell propagator does not account for non-Keplerian accelerations by default but does accept a user-defined function that can be called at each time step to generate the accelerations for the second term of Eq. 3.1. This allows the user to customize the propagator's perturbation model. The MAPS propagator accounts for the J2 perturbation as well as the gravitational effects of the Sun and Moon. The accelerations due to each of these perturbations are calculated separately using the J2 and three-body models in the `poliastro.core.propagation` module. Then they are added together and returned to the Cowell propagator. For each timestamp the propagator receives, it returns the satellite's state vectors in Cartesian GCRS coordinates.

Since `poliastro` does not support propagation in reference frames other than GCRS or transformations between coordinate representations, MAPS uses its own `GEOsat_Orbit` class to format and catalog information about the satellite's orbit and state history that `poliastro` objects cannot retain. The MAPS propagator is accessible as a `GEOsat_Orbit` class method so that as an orbit is propagated, the resulting GCRS state vectors are automatically associated with the orbit from which they were generated. State vectors are accessible as a class attribute in their original format, but they are also converted to other reference frames and stored as additional attributes. These transformations are accomplished using `astropy` coordinates which support numerous representation and reference frame transformations. Through the `GEOsat_Orbit` class, MAPS accesses the satellite's position as Cartesian GCRS coordinates and as spherical ITRS coordinates that provide the ECEF latitude and longitude.

3.2.3 Generating Spatial Probability Distributions

MAPS uses the `Probability_at_time` function to simulate spatial probability distributions via Monte Carlo sampling. It accepts a run time, maneuver model, and initial state, and returns a `Probability` class object. When executing this function, MAPS propagates the satellite's orbit from the same initial state and to the same observation time for every iteration of the Monte Carlo simulation, but at the beginning of each run the maneuver time and ΔV components are randomly sampled from the `maneuver_profile` input as described in Section 3.2.1. The initial orbit is propagated to the sampled maneuver time, at which point the velocity components are added to the most recent state vector, and the new state is propagated to the end of the simulation window.

MAPS calculates the satellite's final position in the ITRS frame from the GCRS coordinates returned by the propagator. Both sets of coordinates are appended to their respective `GEOsat_Orbit` attribute arrays. After this is repeated for the specified number of samples, the two position vector arrays and the final observation timestamp are used to instantiate a `Probability` class object. Finally, the propagator is called on the set of true maneuver parameters defined in the `maneuver_profile` to determine the satellite's true position at the observation time, and the resulting vector is instantiated as an attribute of the `Probability` object which is then returned. The `Probability` class has several methods that can be used to plot the posterior spatial probability distribution as well as the sampled satellite positions in multiple reference frames and from specific viewpoints.

3.2.4 MAPS Plot Views

Probability Density Functions

Upon its return, a probability object can be used to plot the probability density function of the satellite's position at the observation time by calling the class method `plot_PDF`. This function calculates the mean and standard deviation of the distance between the samples and the satellite's true position. These values are then used to

calculate and plot the probability of each sample according to a Gaussian distribution model. If this method is called before a location is assigned to the observation point, then the resulting distances are calculated from the array of GCRS coordinates and are given in units of kilometers. Otherwise, distance is given in degrees and corresponds to an angular separation calculated from ITRS coordinates. Probability density plots also display the mean value of the distribution as a fraction of its standard deviation.

Spatial Distributions in Two and Three Dimensions

MAPS can display the distribution of predicted satellite positions as a 3D scatter plot or as a 2D projection. Three-dimensional plots use GCRS coordinates. They do not require additional specifications beyond those automatically associated with MAPS-generated `Probability` objects and can be accessed using the `plot_3D` method. In this plot view, the sampled data points are color-coded according to their distance from the satellite's true location as shown in Figure 3-5.

Before plotting the `Probability` class's two-dimensional projection of a spatial distribution, the location of the observer must be specified so that the satellite's coordinates can be converted from ITRS to an azimuth angle - which is measured along the horizon - and an elevation angle - which is measured vertically from the horizon. The observation point may be instantiated as a class attribute from its ITRS coordinates using the `from_location` method or passed directly to the `plot_from_location` method which generates the plot view. These functions create an Astropy `EarthLocation` object which can then be used to convert GCRS or ITRS coordinates into the proper viewing frame for its associated location.

Optionally, the user can provide the location of a nearby object at the observation time using the `object_intersection` method. This location must be given in ITRS coordinates, but MAPS calculates its angular distance from the location of the distribution's mean. This value may also be set directly using the `set_max_degrees` method. To simulate an intersection with another satellite, MAPS flags any sample separated from the mean position by more than half of this distance as high risk. This emulates an encroaching second object with a comparable spatial distri-

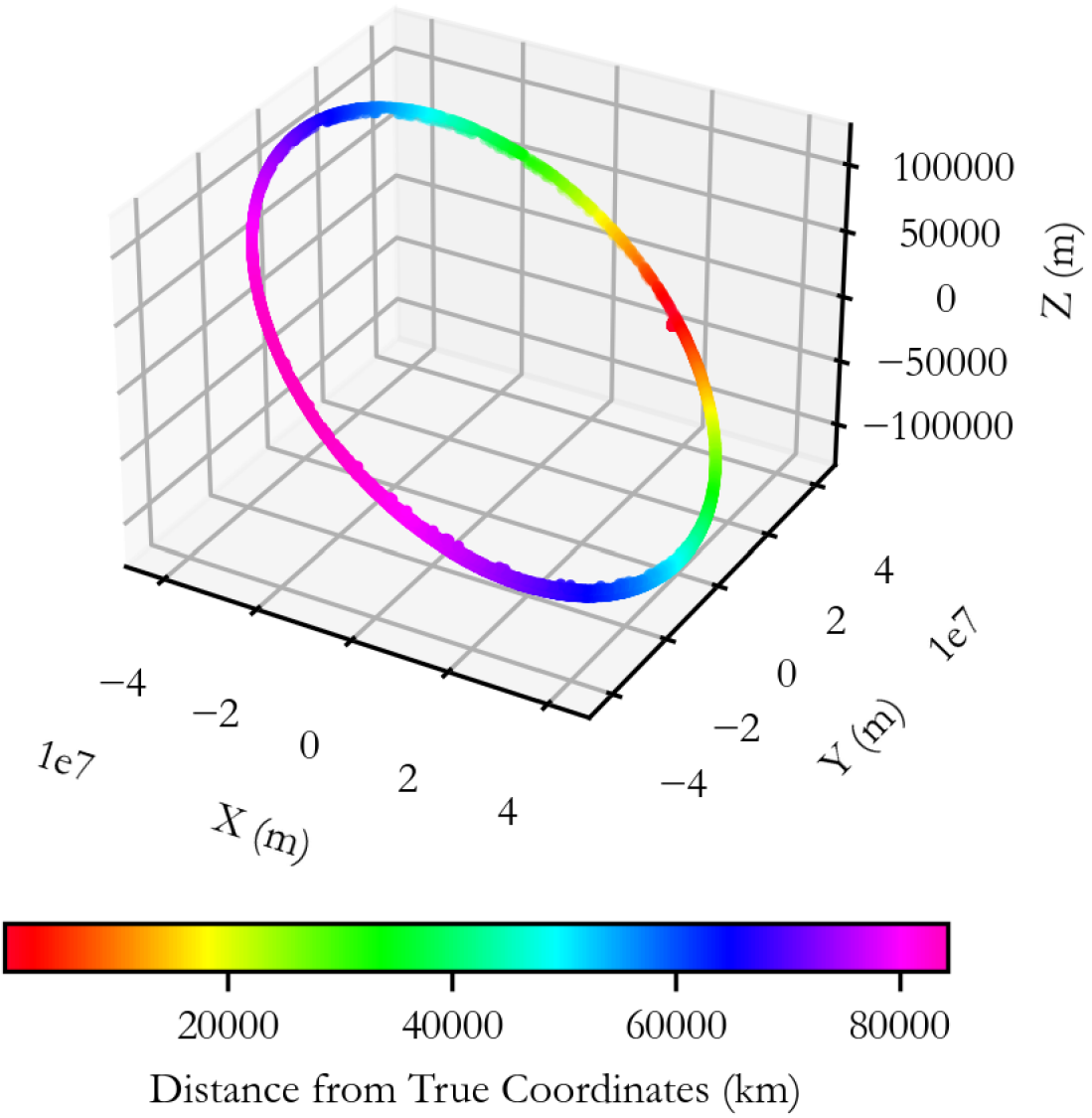

Figure 3-5: **MAPS 3D GCRS plot view.** 3D visualization of a large spatial distribution for a GEO satellite. Colors indicate the discrepancy between each sample and the satellite's true position.

bution. If the intersection distance is initialized before plotting the 2D projection, `plot_from_location` uses a dual color scheme to differentiate the high-risk samples from the rest of the distribution. Low-risk data is shown in black, and high-risk data is colored a light gray. This allows users to easily see which portions of the distribution can be expected to correspond to a high risk of cross-tagging without having to run another Monte Carlo simulation for a second satellite.

Sensor Field-of-View and Resolution Constraints

To account for additional viewing constraints, users may provide a specific FOV and resolution for a ground-based sensor located at the observation point. The FOV must be entered in units of degrees, and resolution is expressed in terms of the pixel scale in units of arc seconds. These values may be passed to the `from_sensor` class method or directly to the `plot_from_sensor` method that generates the constrained plot view. These functions isolate the samples that would be visible to a sensor with its FOV centered at the mean of the spatial distribution. When the `plot_from_sensor` method is called, these samples are sorted into a 2D histogram with bins scaled to the same dimensions as the sensor's pixels. The resulting plot view is demonstrated in Figure 3-6 and includes a pixelated representation of the isolated samples with pixel brightness that increases with a bin's sample density. In this plot view, it is relevant to note that the color is scaled relative to the sample density observed within the FOV only, not the entirety of the distribution.

If the satellite's true position is within the FOV, its location is marked in the plot by a red triangle. It is possible that the full spatial distribution is very large or very small compared to the sensor's FOV, and that the relative size is not apparent from either plot view. In this case, the `plot_from_location` method may be called with its `FOV` parameter enabled. By default, this boolean is false, but when enabled, the `plot_from_location` view encloses the region displayed by the pixelated FOV in a green rectangle to provide a reference for scale.

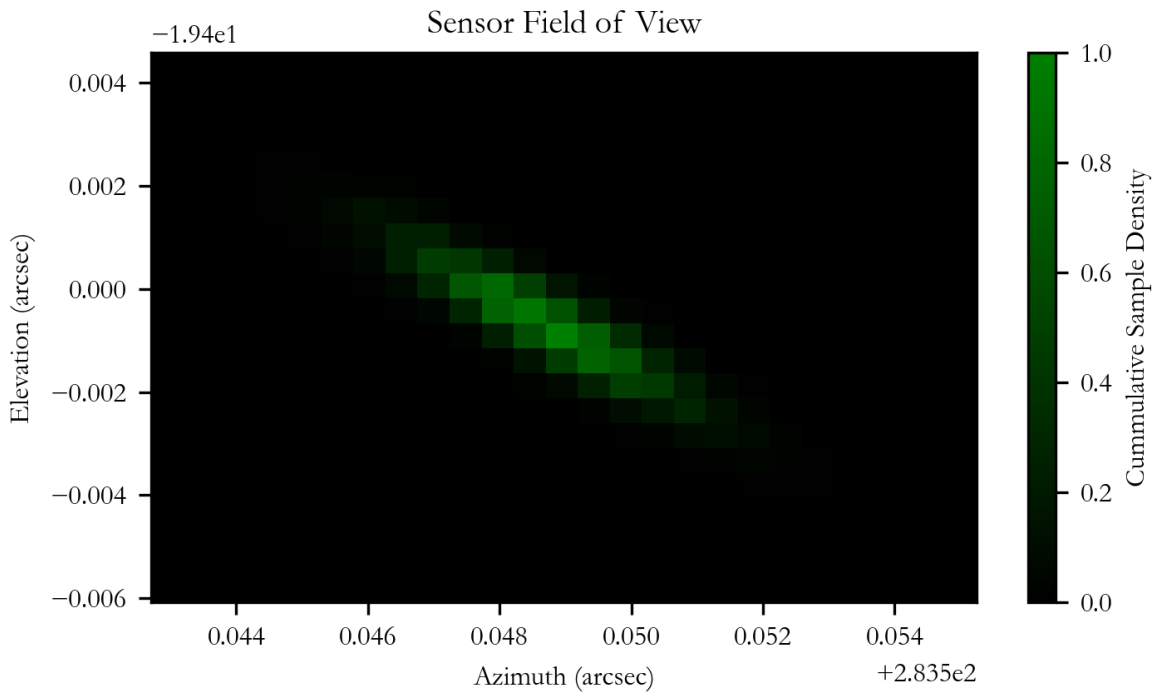

Figure 3-6: **Example of MAPS plot view for sensor FOV and resolution constraints.** The plot is centered at the mean of the spatial distribution and scaled to the user-defined sensor FOV. MAPS determines pixel size from the provided value for pixel scale, and pixel brightness is normalized to the maximum sample density within the FOV.

3.3 Evaluating Maneuver Predictions for Clustered Satellites

This section demonstrates how MAPS might be used to evaluate maneuver predictions for satellites like those in the ASTRA 19.2°E cluster. Three maneuver profiles for a single East-West station-keeping maneuver are tested, each with a different maneuver time accuracy and precision. Section 3.3.6 interprets and compares the results of each MAPS evaluation.

3.3.1 Simulating Truth Trajectories

For the purposes of this study, a truth trajectory was simulated based on a segment of *ASTRA 1N*'s (Satellite ID: 37775) state history to represent realistic values for station-keeping ΔV. As shown in Figure 3-7, the TLE-sourced state history for the chosen time period included a single East-West station-keeping maneuver and several North-South maneuvers. Since the North-South maneuvers were executed very consistently, only the East-West maneuver was implemented in the simulated trajectory. The simulation and true maneuver parameters for this trajectory may be found in Table 3.1. Since the ASTRA 19.2°E cluster is operated by SES, the SES head office in Luxembourg was designated as the observation point. Then, using the distances presented in Figure 1-5, the median distance between *ASTRA 1M* (Satellite ID: 33436) and *ASTRA 1N* was set as the risk threshold for cross-tagging.

3.3.2 Simulating Maneuver Profiles

As discussed in Section 3.2.1, MAPS maneuver profiles consist of the maneuver's true time and ΔV components in combination with the mean and standard deviation of the modeled probability distributions for these four parameters. To simulate multiple maneuver profiles for the trajectory discussed in Section 3.3.1, the means for the modeled distributions were generated by adding offsets to the corresponding true value of each maneuver parameter shown in Table 3.1. The mean maneuver time

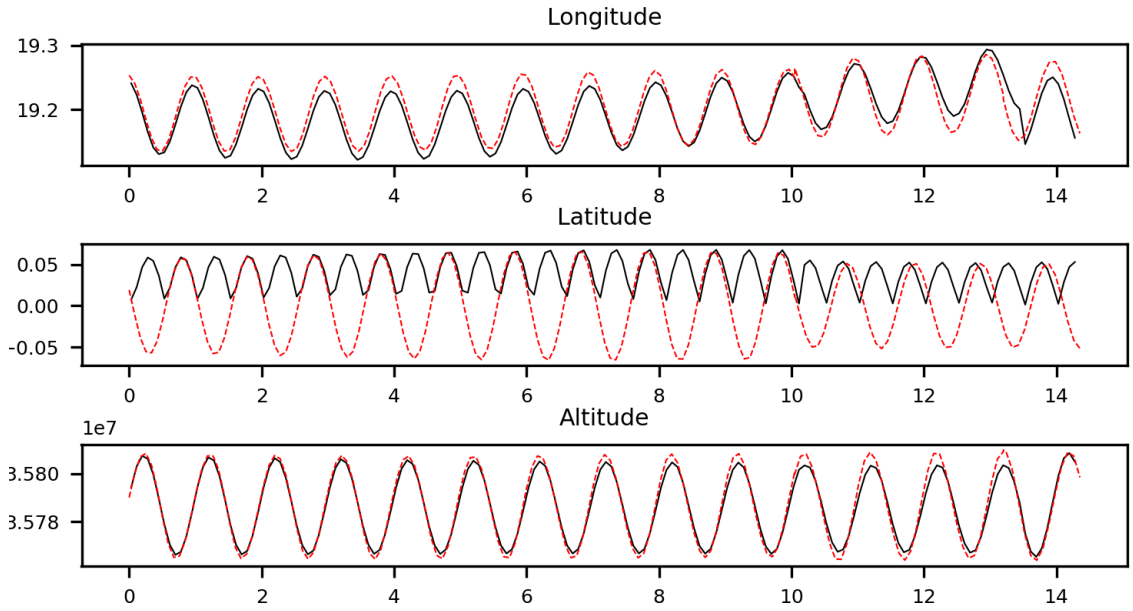

Figure 3-7: **Trajectory simulation for *ASTRA 1N* (Satellite ID: 37775).** Simulated GEO satellite trajectory (red) based on a TLE-sourced segment of the geographic positional history for *ASTRA 1N* (Satellite ID: 37775) (black).

Initial Timestamp	2021-07-02 15:16:06.234
Initial Position (GCRS)	[-41377348.81401046, 8127831.26850074, 99280.29437476] m
Initial Velocity (GCRS)	[-594.079711889208, -3016.503082643794, -1.689834987744] m/s
Run Time	1,095,120 seconds ≃ 12.675 days
True Maneuver Time	868,320 seconds ≃ 10.05 days
True ΔV (GCRS)	[-0.023, 0.0023, 0.9] m/s
Number of Samples	10,000

Table 3.1: **MAPS truth inputs and static simulation parameters.**

	Case 1	Case 2	Case 3
Mean Maneuver Time	867,789 seconds	866,199 seconds	864,078 seconds
Mean ΔV (GCRS)	[-0.023028380797, 0.002332346217, 0.903025508725] m/s	[-0.023028380797, 0.002332346217, 0.903025508725] m/s	[-0.023028380797, 0.002332346217, 0.903025508725] m/s
Standard Deviation of Maneuver Time	2,961 seconds	51,401 seconds	80,366 seconds
Standard Deviation of ΔV (GCRS)	[0.00042546599, 0, -0.01911918069] m/s	[-0.00015662277, -0.00019119181, -0.01307715887] m/s	[0.00042546599, 0, -0.01911918069] m/s

Table 3.2: **Prior distribution parameters for MAPS maneuver profile inputs.**

offsets were sampled from within the ranges of 15 minutes, one hour, and two hours for cases 1, 2, and 3 respectively. The standard deviations for the maneuver time distributions were then randomly sampled from ranges of one hour, 24 hours, and 36 hours to avoid any potential dependencies on orbit symmetry. These values were chosen to reflect typical variations in maneuver frequency for a few common station-keeping schemes. The offsets and standard deviations for the ΔV distributions were selected to be negligible. In fact, all of the time and maneuver offsets were chosen to be relatively small so that the true satellite location could be incorporated into the demonstrations of each plot view. The complete list of maneuver profile components may be found in Table 3.2.

For clarity, the maneuver profiles may be referenced as high-precision for case 1, moderate-precision for case 2, and low-precision for case 3. These terms refer to the prior distribution for maneuver time and are meant to distinguish the simulated prediction models relative to each other. They are not intended to be representative of a comparative performance to maneuver prediction models in general.

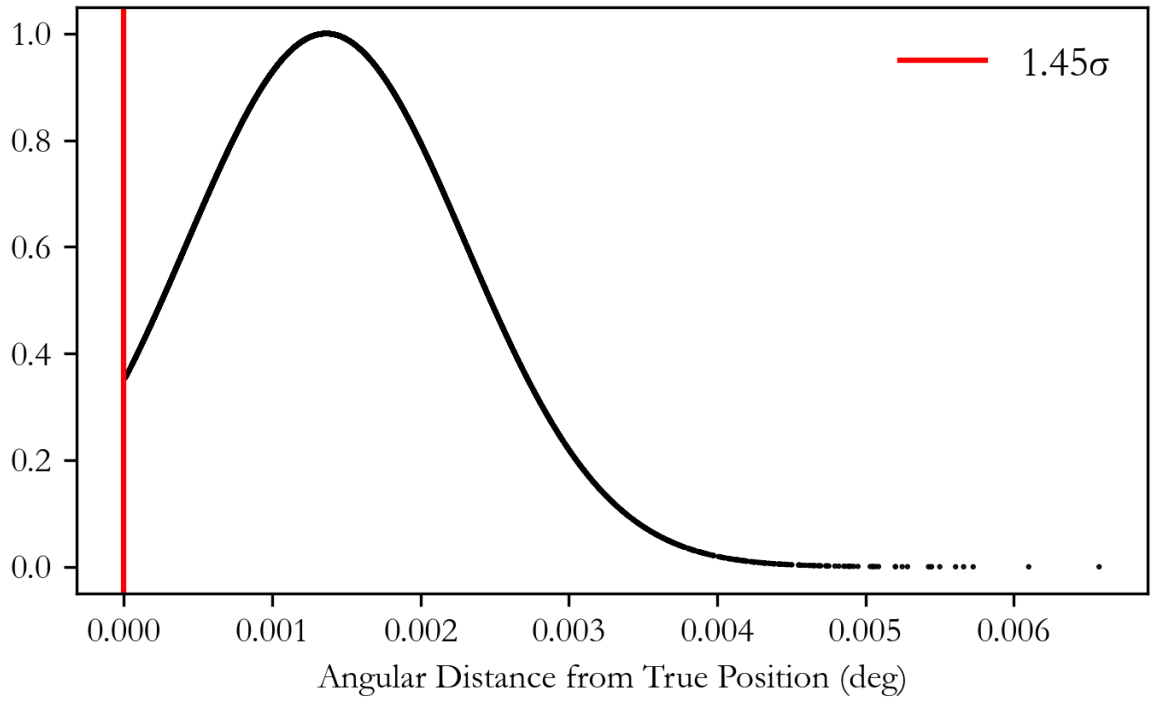

Figure 3-8: **Spatial probability distribution of a high-precision maneuver prediction.** MAPS probability distribution for the angular distance from the satellite's true position as predicted from a high-precision maneuver profile. The distribution's standard deviation is 0.00094° which is very low, indicating that the model is effective for this use case.

3.3.3 Case 1: Plot Views for a High-precision Model

The mean of the high-precision maneuver time distribution was offset from the true maneuver time by approximately nine minutes with a standard deviation of around 50 minutes. According to Figure 3-8, the corresponding mean offset in the PDF was approximately $0.0014°$ or 1.45σ in terms of the distribution's standard deviation. The model performs very well for this use case. Figure 3-9 shows that the cluster of sampled positions at the observation time is constrained to a tight pattern surrounding the satellite's true position. In fact, the entire distribution falls within $0.007°$ of this location which is well below the risk threshold of $0.05°$. Figure 3-10a displays a $0.98°$ FOV for a sensor with a pixel scale of 0.78" [13]. As a result of this prediction model's high time precision, the distribution is too small to be visible at the scale of the FOV plot. The magnified view in Figure 3-10b shows that the entire distribution envelops no more than a few dozen pixels and that the satellite's true position falls between two of the highest-density pixels. This placement indicates that under these conditions, the sensor would locate the satellite within one pixel of the location derived from the prediction model.

3.3.4 Case 2: Plot Views for a Moderate-precision Maneuver Profile

In the moderate-precision maneuver profile, the time distribution's mean was offset from the true maneuver time by approximately 35 minutes, and its standard deviation was 14 hours. As shown in Figure 3-11, this corresponds to a mean offset in the probability distribution of approximately $24°$ or 0.51σ. Spatial distributions that follow a pattern like the one in Figure 3-12a appear similar to the orbit shape in Figure 3-5 when viewed in three dimensions. The distribution wraps around the geostationary belt, looping back on itself, and only the small portion indicated by Figure 3-12 is captured by the FOV in Figure 3-13a. The enlarged view in Figure 3-13b shows that a section of the distribution, including the location predicted from the mean maneuver parameters, intersects the satellite's true location. In this case, due to

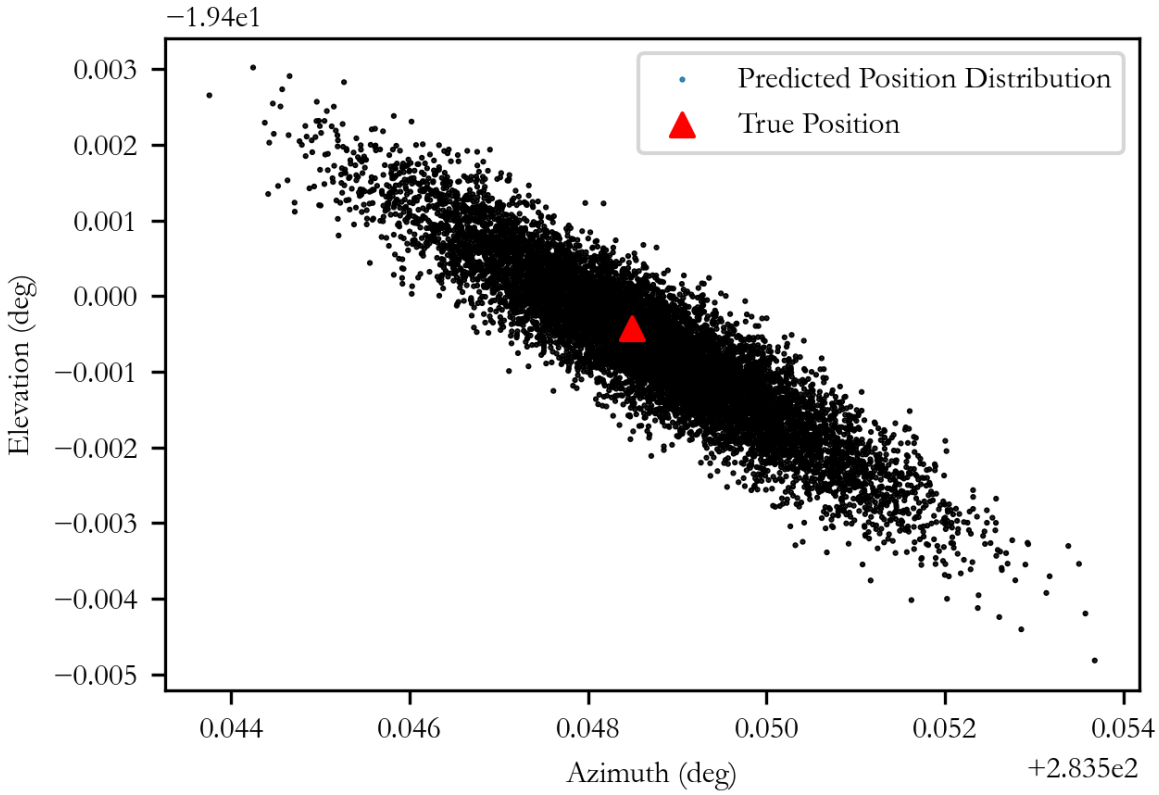

Figure 3-9: **Elevation-Azimuth projection of satellite positions sampled from a high-precision maneuver prediction model.** Two-dimensional, observer-dependent projection of a tight spatial distribution with a negligible offset from the true satellite position.

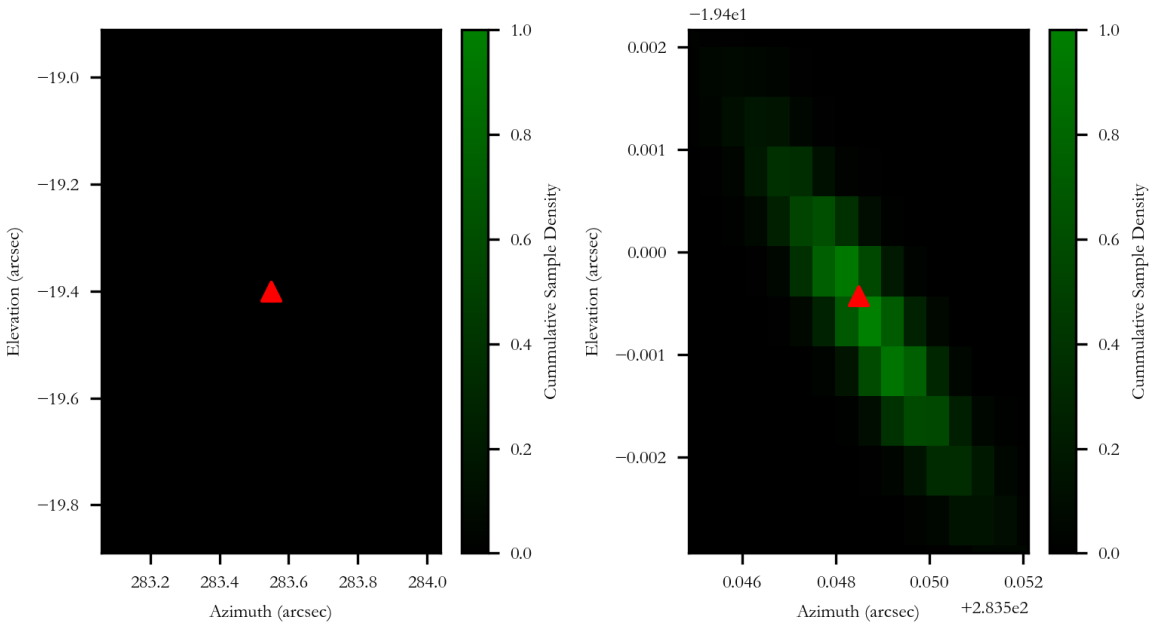

(a) (b)

Figure 3-10: **Sensor FOV for a high-precision maneuver profile.** (a) MAPS-generated FOV for a distribution derived from a high-precision maneuver profile. The sensor is centered on the sample generated by the mean maneuver parameters. (b) Enlarged view of the satellite's true position within the sensor's FOV.

the small offset between the mean and true maneuver times, the sensor would be able to locate the satellite within a few arc seconds of its predicted location. However, due to its large standard deviation, this model is not suitable for predicting maneuvers over this timescale, especially not in GEO satellite clusters. As demonstrated by Figures 3-11 and 3-12, only a minuscule portion of the distribution remains below the risk threshold for cross-tagging.

3.3.5 Case 3: Plot Views for a Low-precision Model

The mean maneuver time in the low-precision profile was offset from the true maneuver time by approximately 70 minutes, and the respective distribution had a standard deviation of 22 hours. This translates to a mean distance offset of approximately 32° or 0.62σ as shown in Figure 3-14. The corresponding spatial distribution is shown in Figure 3-15a. Similarly to the moderate-precision model, this distribution trails the entire GEO belt due to its large standard deviation. Figure 3-15b indicates the

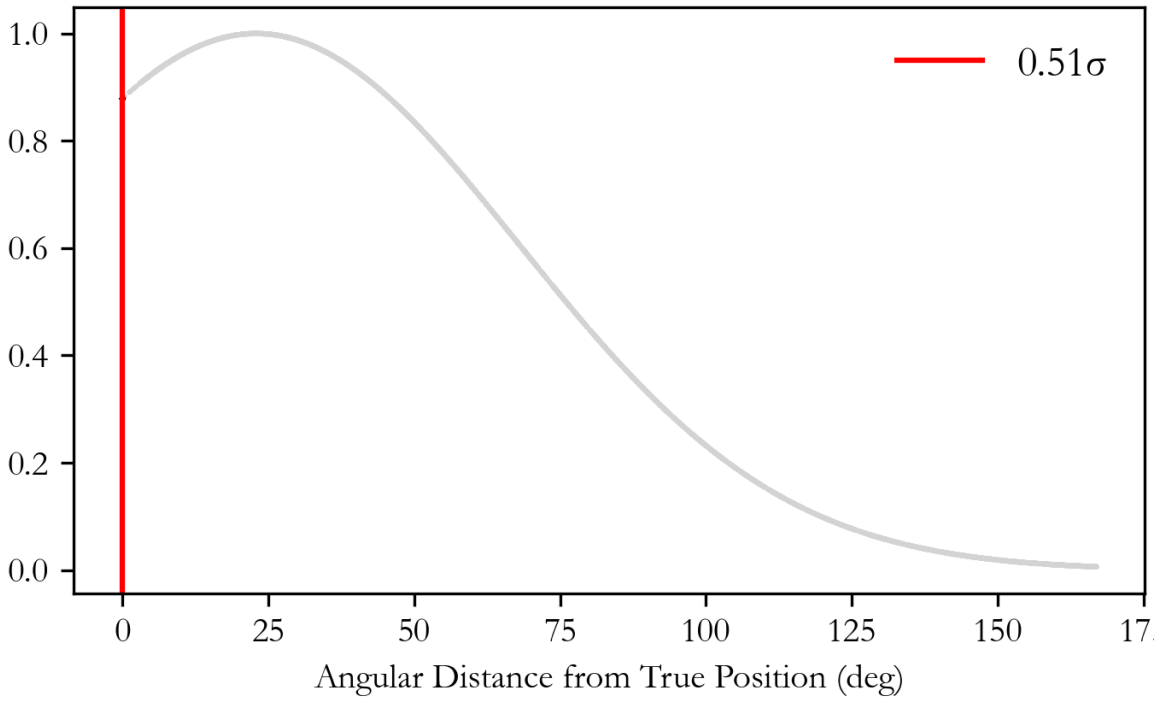

Figure 3-11: **Spatial probability distribution of a moderate-precision maneuver prediction.** MAPS-generated PDF for the angular distance from the satellite's true position as predicted from a moderate-precision maneuver profile. The standard deviation of the distribution is 44.71°, and its angular range is quite large, meaning that the model is not precise enough for this use case.

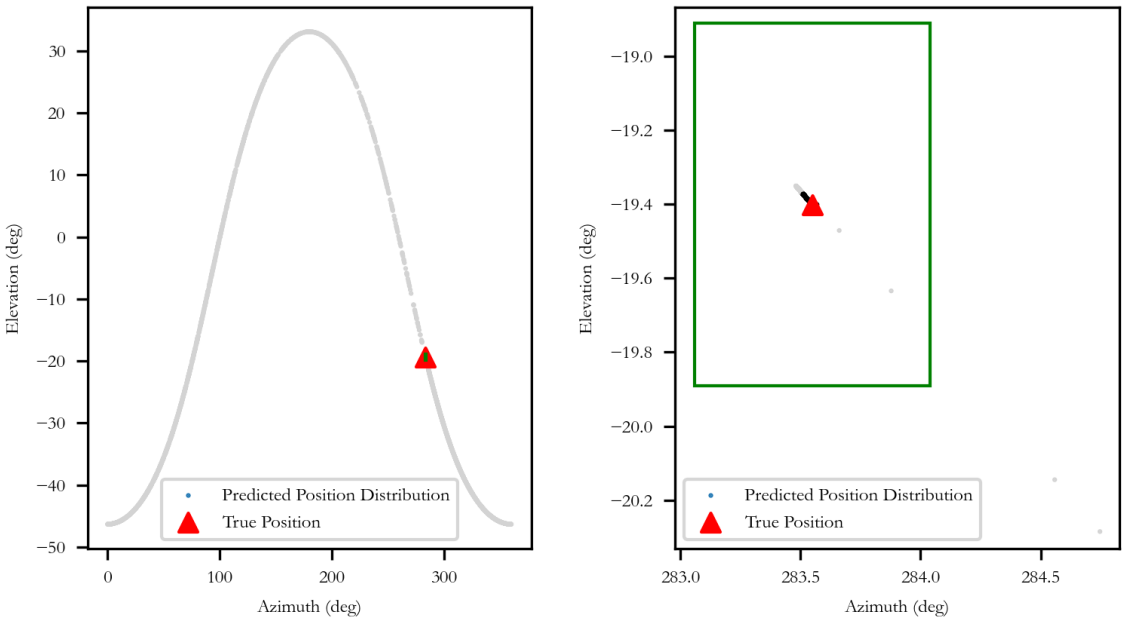

(a) (b)

Figure 3-12: **Elevation-Azimuth projection of satellite positions sampled from a moderate-precision maneuver prediction model.** (a) Two-dimensional, observer-dependent projection of a large spatial distribution. Portions with a high cross-tag risk are colored gray. (b) A small segment of the full spatial distribution is enlarged to show the scale and contents of the sensor FOV (green) plotted in Figure 3-13a.

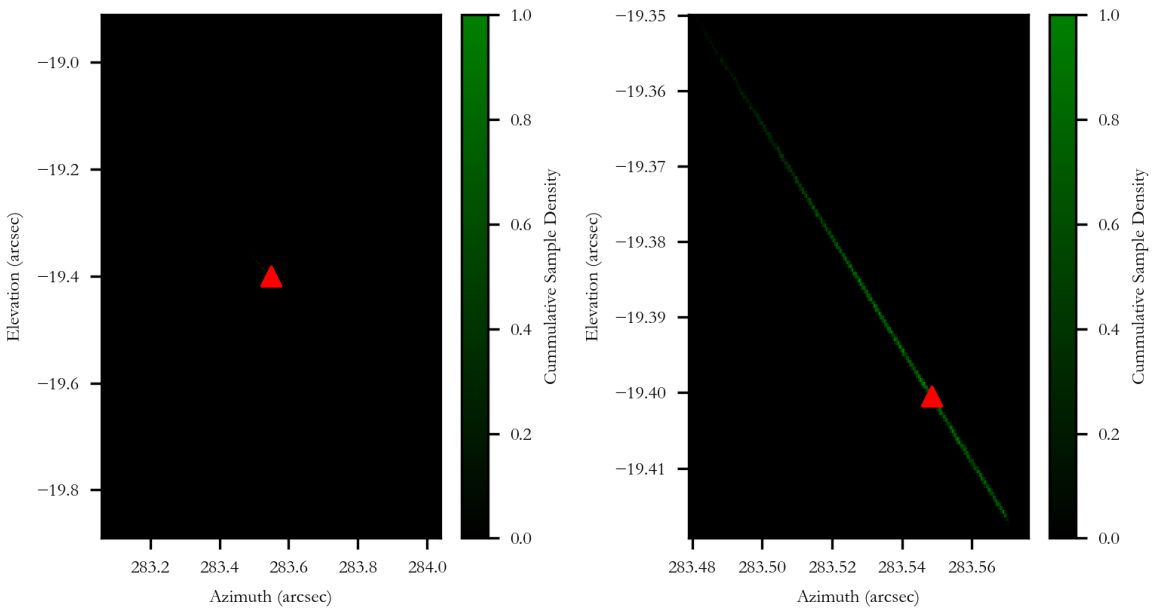

(a) (b)

Figure 3-13: **Sensor FOV for a moderate-precision maneuver profile.** (a) MAPS-generated FOV for a distribution derived from a moderate-precision maneuver profile. The sensor is centered at the sample generated by the mean maneuver parameters. (b) Enlarged view of the satellite's true position within the sensor's FOV.

portion of the distribution captured by the FOV pictured in Figure 3-16a. The 70-minute offset between mean and true maneuver times does not result in a spatial offset large enough to exclude the true position from the FOV plot view, but once again, the standard deviation is too high. The low-precision maneuver profile is not a suitable prediction model for GEO satellites at this simulation timescale.

3.3.6 Comparing Maneuver Prediction Models

MAPS's PDF describes the relationship between each of the satellite's possible locations and the probability value assigned to those locations by the prediction model. MAPS is primarily designed to simplify the task of evaluating the accuracy and precision of prediction models for a specific set of sensor, spatial, and time constraints. The accuracy of the prediction model depends on the probability that the model assigns to the satellite's true location and on the distance between this location and the location where the model predicts that the satellite is most likely to be. Instead of

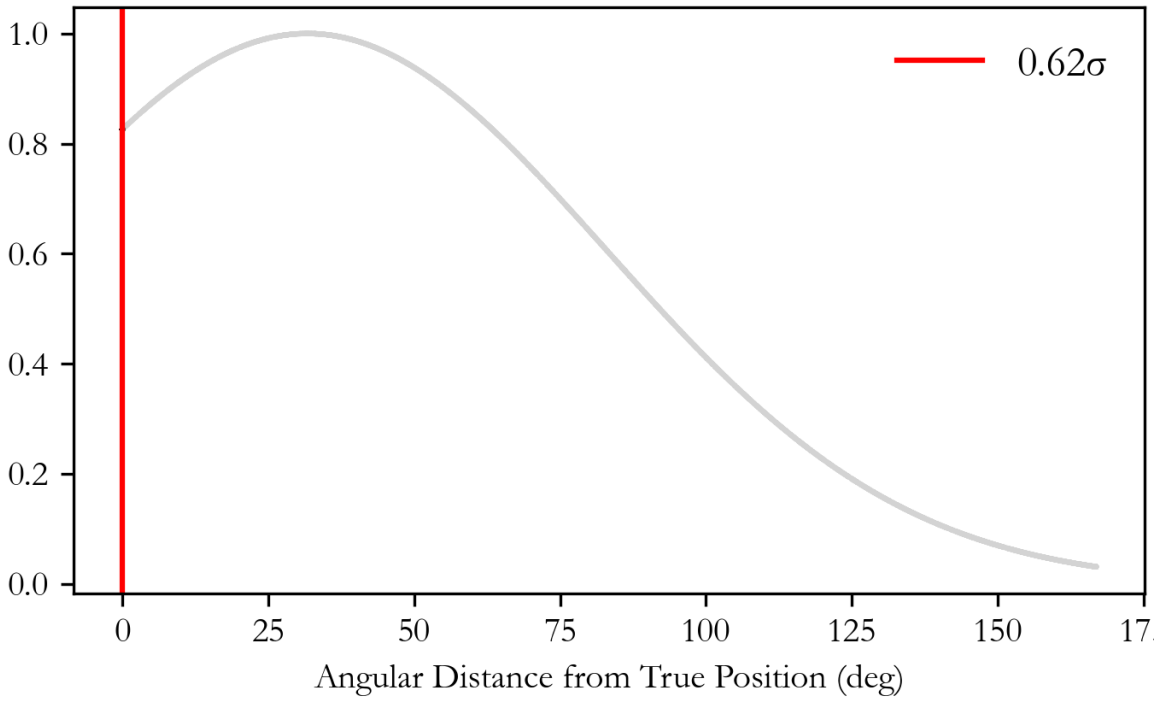

Figure 3-14: **Spatial probability distribution of a low-precision maneuver prediction.** MAPS probability distribution for the angular distance from the satellite's true position as predicted from a low-precision maneuver profile. The standard deviation is 50.98°. This value is far to high to meet the precision requirements for maneuver detection in the GEO regime.

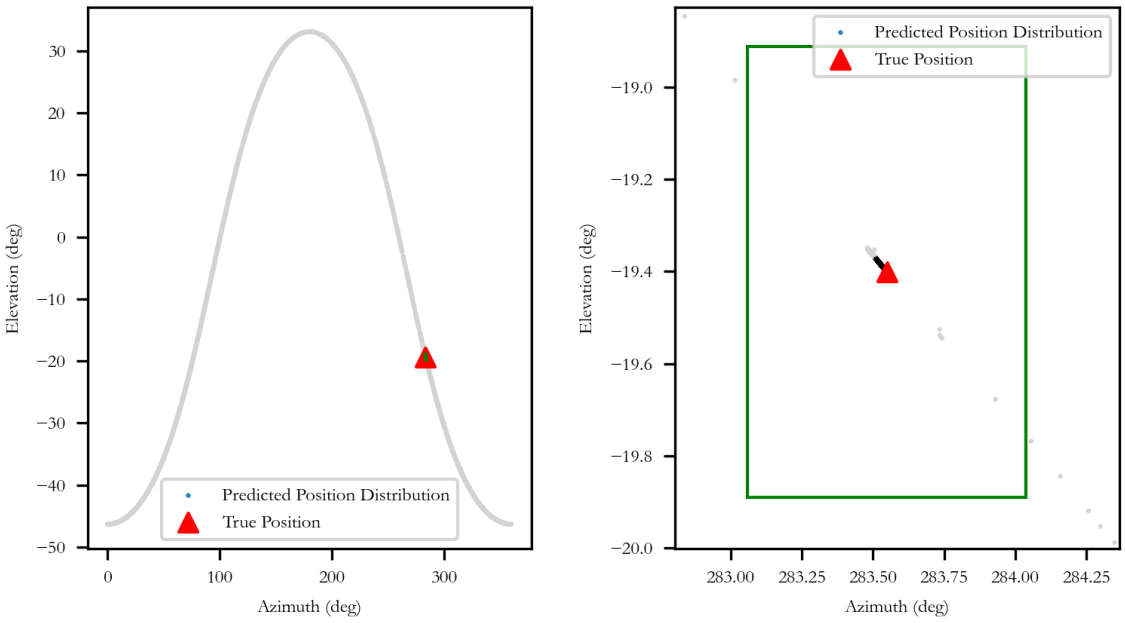

(a) (b)

Figure 3-15: **Elevation-Azimuth projection of satellite positions sampled from a low-precision maneuver prediction model.** (a) Two-dimensional, observer-dependent projection of a large spatial distribution. Portions with a high cross-tag risk are colored gray. (b) Small segment of the full spatial distribution enlarged to show the scale and contents of the sensor FOV (green) plotted in Figure 3-16a.

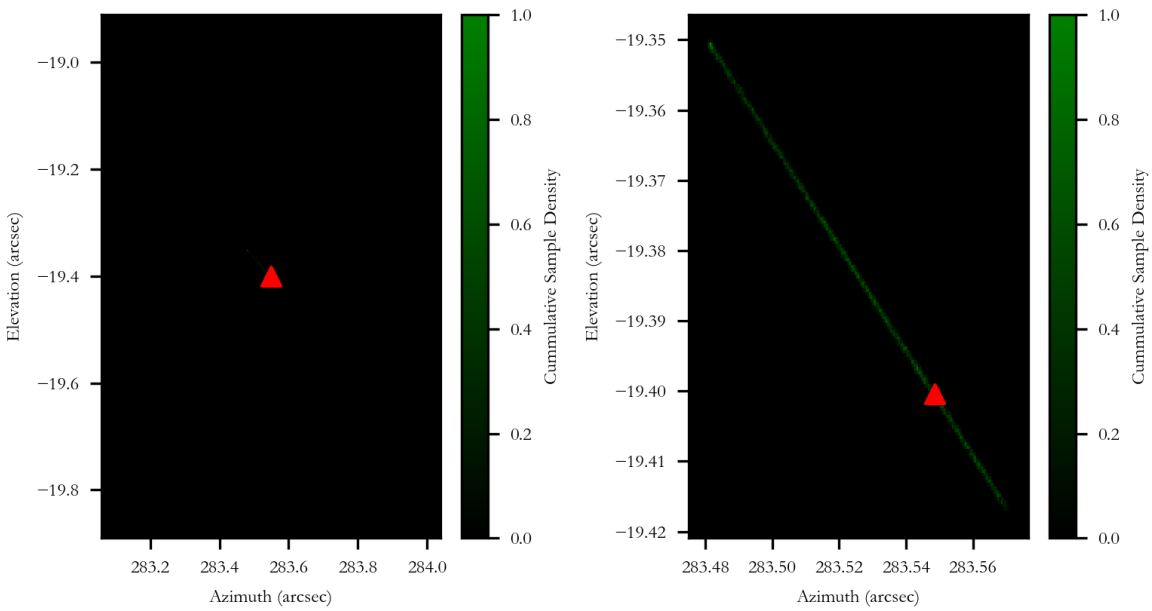

(a) (b)

Figure 3-16: **Sensor FOV for a low-precision maneuver profile.** (a) MAPS-generated FOV for a distribution derived from a low-precision maneuver profile. The sensor is centered at the sample generated by the mean maneuver parameters. (b) Enlarged view of the satellite's true position within the sensor's FOV.

plotting the probability distribution in two or three-dimensional coordinates, MAPS simply plots the probability as a function of the distance between the satellite's possible locations and its true location at the final observation time. This allows the user to see how confidently the model can predict the satellite's location and whether or not this confidence is suitably scaled for the FOV of their sensor. The standard deviation of this simplified PDF provides a metric for model precision. Incorporating a secondary object to identify conditions with a higher risk of cross-tagging is another way to determine whether or not the accuracy and precision of a model are high enough to accommodate a certain use case.

Out of the three test cases, only the first prediction model was able to predict the satellite's location with enough precision to confidently avoid cross-tagging. There was no apparent risk since the full spatial distribution fell within the FOV and the intersection distance. The second maneuver profile had a mean time offset almost four times the offset of the first, and the third distribution's time offset was double

the second. Despite this, all three models were spatially centered within the area of acceptable risk surrounding the satellite's true location. It was due to their high standard deviations that the moderate and low-precision profiles resulted in distributions that were not probabilistically focused within the region of acceptable risk. The standard deviation component of the maneuver profiles had a disproportionately high impact on the posterior distributions compared to the effects of the varied maneuver time offsets. The standard deviation of the second maneuver time distribution was 14 times higher than the first, and this resulted in a $4,756,300\%$ increase in the standard deviation of the spatial distribution where offsetting the time distribution mean only shifted the spatial mean by a few arc-seconds. This is consistent with the offset relationship demonstrated in Figure 1-4 and is due to the geometry of the orbit. In these simulations, the time and magnitude offsets were chosen to be very small for the purpose of retaining a visual reference for the true satellite position in each of the plot views. However, in such cases where the standard deviations of the prior distributions are very large, the models generate proportionately low-confidence predictions.

Since many GEO satellite maneuver schedules contain inconsistencies far beyond the scope of a single day, the poor performance of the second and third models is a perfect example of why maneuver prediction is so difficult. Even the distribution generated from the high-precision maneuver profile does not entirely satisfy the distance constraints characterized in Chapter 1 for ASTRA 19.2°E. In fact, its performance is orders of magnitude short of resolving the minimum operational distance between *ASTRA 1N* and *ASTRA 1M* which spans only four pixels for a sensor with a pixel scale of 0.78". ASTRA 19.2°E is not the only cluster whose satellites operate in such close proximity, and proximity operations are only one of the many challenges associated with maneuver prediction and satellite tracking. However, MAPS has the capability to mitigate some of these challenges. As demonstrated by the results of the three prediction model analyses, MAPS can provide the context necessary to assess prediction model accuracy and precision for different satellites, cluster formations, and sensor specifications. Its PDF function provides a simple plot view of model

performance, and its spatial distributions and FOV plots help users to visualize the practical limitations of viewing GEO satellites from ground-based sensors so that even researchers who are not familiar with instrumentation or raw observations can contextualize the level of benefit that a prediction model can realistically provide.

Chapter 4

Conclusion

4.1 Contributions

Understanding GEO satellite behavior and control objectives is a challenging aspect of SSA, largely due to the variations inherent to GEO station-keeping routines. PoL characterization across the GEO regime can establish precedent to improve behavior recognition and prediction capabilities, but this requires analyzing large amounts of data. Additionally, current research efforts are poorly aligned and literarily disconnected due to discrepant jargon. This work introduced two tools designed to support SSA research in these areas through computationally efficient PoL characterization and contextualizing maneuver prediction models.

The first tool, SNICT, identifies and classifies nodes according to a versatile PoL model for the purpose of enabling broader characterization of GEO behavioral modes and contextualizing new satellite behaviors [52]. SNICT's simple node-detection algorithm was presented and tested on TLE-derived longitudinal position histories for a diverse group of 18 GEO satellites. Overall, there was an 83% node correlation between the algorithmic detections and the truth data and upwards of 89% correlation for the large, node-dense histories that comprise the algorithm's ideal use case. This outcome is promising considering the low level of complexity involved in this node detection method and the poor quality of the TLE source data.

The second tool, MAPS, simplifies the task of evaluating the accuracy and pre-

cision of maneuver prediction models for a specific set of sensor, spatial, and time constraints. Three probabilistic prediction models were tested in a surveillance scenario representative of a realistic FOV, optical sensor resolution, and satellite cluster behavior. The performance of these predictions was analyzed from MAPS-generated spatial probability plots, revealing that only one of the three models met the precision requirements for the scenario's sensor and inter-satellite distance. The results demonstrated the practical limitations of ground-based satellite tracking and provided a simple metric for evaluating the efficacy of each prediction model for this use case.

4.2 Future Work

The PoL model nomenclature proposed in Chapter 2 is generalizable across SSA research objectives and can support expanded analysis of satellite behavioral modes such as stratification of station-keeping schemes and strategic satellite characterization. SNICT demonstrated a consistent ability to correctly isolate behavioral modes with a relatively high percentage of directly correlated node detections considering the sparsity and large imperfections in the source data. Additional node detection filtering would enhance the accuracy and robustness of node classification, especially in the case of AD nodes. Alternative data sources have not been tested but can be easily integrated with SNICT since the algorithm only depends on derived longitudinal position histories, not the source-data format. To determine the impact of data quality, SNICT's performance should be evaluated for additional data sources and compared to the results of the TLE-based analysis.

As a more complicated system, MAPS's functionality has the potential to be improved in many areas moving forward. In the short term, incorporating support for additional sensor configurations, reference frames, and maneuver profile formats would expand the tool's effective user base. Also, though technically supported by MAPS's current infrastructure, simulations for space-based surveillance can be tested as an alternative to ground-based telescope views [1]. In the long term, MAPS would benefit from transitioning away from the poliastro propagation framework since it

imposes limitations on maneuver modeling and coordinate frames. Furthermore, the impact of both MAPS and SNICT could grow from expansion to other orbital regimes and integration with larger surveillance frameworks.

Bibliography

[1] Mark R. Ackermann, David D. Cox, Rex R. Kiziah, Peter C. Zimmer, John T. McGraw, and David D. Cox. A systematic examination of ground-based and space-based approaches to optical detection and tracking of artificial satellites. Technical Report SAND2015-3726C, Sandia National Lab, 5 2015.

[2] Airbus. All-electric propulsion satellites. Airbus Newsroom, June 2017.

[3] ARCLab-MIT. GEO-Toolbox.

[4] Astropy Collaboration, A. M. Price-Whelan, B. M. Sipőcz, H. M. Günther, P. L. Lim, S. M. Crawford, S. Conseil, D. L. Shupe, M. W. Craig, N. Dencheva, A. Ginsburg, J. T. VanderPlas, L. D. Bradley, D. Pérez-Suárez, M. de Val-Borro, T. L. Aldcroft, K. L. Cruz, T. P. Robitaille, E. J. Tollerud, C. Ardelean, T. Babej, Y. P. Bach, M. Bachetti, A. V. Bakanov, S. P. Bamford, G. Barentsen, P. Barmby, A. Baumbach, K. L. Berry, F. Biscani, M. Boquien, K. A. Bostroem, L. G. Bouma, G. B. Brammer, E. M. Bray, H. Breytenbach, H. Buddelmeijer, D. J. Burke, G. Calderone, J. L. Cano Rodríguez, M. Cara, J. V. M. Cardoso, S. Cheedella, Y. Copin, L. Corrales, D. Crichton, D. D'Avella, C. Deil, É. Depagne, J. P. Dietrich, A. Donath, M. Droettboom, N. Earl, T. Erben, S. Fabbro, L. A. Ferreira, T. Finethy, R. T. Fox, L. H. Garrison, S. L. J. Gibbons, D. A. Goldstein, R. Gommers, J. P. Greco, P. Greenfield, A. M. Groener, F. Grollier, A. Hagen, P. Hirst, D. Homeier, A. J. Horton, G. Hosseinzadeh, L. Hu, J. S. Hunkeler, Ž. Ivezić, A. Jain, T. Jenness, G. Kanarek, S. Kendrew, N. S. Kern, W. E. Kerzendorf, A. Khvalko, J. King, D. Kirkby, A. M. Kulkarni, A. Kumar, A. Lee, D. Lenz, S. P. Littlefair, Z. Ma, D. M. Macleod, M. Mastropietro, C. McCully, S. Montagnac, B. M. Morris, M. Mueller, S. J. Mumford, D. Muna, N. A. Murphy, S. Nelson, G. H. Nguyen, J. P. Ninan, M. Nöthe, S. Ogaz, S. Oh, J. K. Parejko, N. Parley, S. Pascual, R. Patil, A. A. Patil, A. L. Plunkett, J. X. Prochaska, T. Rastogi, V. Reddy Janga, J. Sabater, P. Sakurikar, M. Seifert, L. E. Sherbert, H. Sherwood-Taylor, A. Y. Shih, J. Sick, M. T. Silbiger, S. Singanamalla, L. P. Singer, P. H. Sladen, K. A. Sooley, S. Sornarajah, O. Streicher, P. Teuben, S. W. Thomas, G. R. Tremblay, J. E. H. Turner, V. Terrón, M. H. van Kerkwijk, A. de la Vega, L. L. Watkins, B. A. Weaver, J. B. Whitmore, J. Woillez, V. Zabalza, and Astropy Contributors. The Astropy Project: Building an Open-science Project and Status of the v2.0 Core Package. *The Astronomical Journal*, 156(3):123, September 2018.

[5] Astropy Collaboration, Adrian M. Price-Whelan, Pey Lian Lim, Nicholas Earl, Nathaniel Starkman, Larry Bradley, David L. Shupe, Aarya A. Patil, Lia Corrales, C. E. Brasseur, Maximilian Nöthe, Axel Donath, Erik Tollerud, Brett M. Morris, Adam Ginsburg, Eero Vaher, Benjamin A. Weaver, James Tocknell, William Jamieson, Marten H. van Kerkwijk, Thomas P. Robitaille, Bruce Merry, Matteo Bachetti, H. Moritz Günther, Thomas L. Aldcroft, Jaime A. Alvarado-Montes, Anne M. Archibald, Attila Bódi, Shreyas Bapat, Geert Barentsen, Juanjo Bazán, Manish Biswas, Médéric Boquien, D. J. Burke, Daria Cara, Mihai Cara, Kyle E. Conroy, Simon Conseil, Matthew W. Craig, Robert M. Cross, Kelle L. Cruz, Francesco D'Eugenio, Nadia Dencheva, Hadrien A. R. Devillepoix, Jörg P. Dietrich, Arthur Davis Eigenbrot, Thomas Erben, Leonardo Ferreira, Daniel Foreman-Mackey, Ryan Fox, Nabil Freij, Suyog Garg, Robel Geda, Lauren Glattly, Yash Gondhalekar, Karl D. Gordon, David Grant, Perry Greenfield, Austen M. Groener, Steve Guest, Sebastian Gurovich, Rasmus Handberg, Akeem Hart, Zac Hatfield-Dodds, Derek Homeier, Griffin Hosseinzadeh, Tim Jenness, Craig K. Jones, Prajwel Joseph, J. Bryce Kalmbach, Emir Karamehmetoglu, Mikołaj Kałuszyński, Michael S. P. Kelley, Nicholas Kern, Wolfgang E. Kerzendorf, Eric W. Koch, Shankar Kulumani, Antony Lee, Chun Ly, Zhiyuan Ma, Conor MacBride, Jakob M. Maljaars, Demitri Muna, N. A. Murphy, Henrik Norman, Richard O'Steen, Kyle A. Oman, Camilla Pacifici, Sergio Pascual, J. Pascual-Granado, Rohit R. Patil, Gabriel I. Perren, Timothy E. Pickering, Tanuj Rastogi, Benjamin R. Roulston, Daniel F. Ryan, Eli S. Rykoff, Jose Sabater, Parikshit Sakurikar, Jesús Salgado, Aniket Sanghi, Nicholas Saunders, Volodymyr Savchenko, Ludwig Schwardt, Michael Seifert-Eckert, Albert Y. Shih, Anany Shrey Jain, Gyanendra Shukla, Jonathan Sick, Chris Simpson, Sudheesh Singanamalla, Leo P. Singer, Jaladh Singhal, Manodeep Sinha, Brigitta M. Sipőcz, Lee R. Spitler, David Stansby, Ole Streicher, Jani Šumak, John D. Swinbank, Dan S. Taranu, Nikita Tewary, Grant R. Tremblay, Miguel de Val-Borro, Samuel J. Van Kooten, Zlatan Vasović, Shresth Verma, José Vinícius de Miranda Cardoso, Peter K. G. Williams, Tom J. Wilson, Benjamin Winkel, W. M. Wood-Vasey, Rui Xue, Peter Yoachim, Chen Zhang, Andrea Zonca, and Astropy Project Contributors. The Astropy Project: Sustaining and Growing a Community-oriented Open-source Project and the Latest Major Release (v5.0) of the Core Package. *The Astrophysics Journal*, 935(2):167, August 2022.

[6] Astropy Collaboration, Thomas P. Robitaille, Erik J. Tollerud, Perry Greenfield, Michael Droettboom, Erik Bray, Tom Aldcroft, Matt Davis, Adam Ginsburg, Adrian M. Price-Whelan, Wolfgang E. Kerzendorf, Alexander Conley, Neil Crighton, Kyle Barbary, Demitri Muna, Henry Ferguson, Frédéric Grollier, Madhura M. Parikh, Prasanth H. Nair, Hans M. Unther, Christoph Deil, Julien Woillez, Simon Conseil, Roban Kramer, James E. H. Turner, Leo Singer, Ryan Fox, Benjamin A. Weaver, Victor Zabalza, Zachary I. Edwards, K. Azalee Bostroem, D. J. Burke, Andrew R. Casey, Steven M. Crawford, Nadia Dencheva, Justin Ely, Tim Jenness, Kathleen Labrie, Pey Lian Lim, Francesco Pierfederici, Andrew Pontzen, Andy Ptak, Brian Refsdal, Mathieu Servillat, and Ole Stre-

icher. Astropy: A community Python package for astronomy. *Astronomy and Astrophysics*, 558:A33, October 2013.

[7] Austin Beer and Kameron Simon. Geosynchronous Satellite Maneuver Identification and Characterization using Passive RF Ranging. In *Proceedings of the Advanced Maui Optical and Space Surveillance Technologies Conference (AMOS)*, 2021.

[8] Louardi Beroual, Djamel Benatia, and Nour el Houda Hedjazi. High Thrust Station Keeping Maneuvers for Geostationary Satellites. *International Journal of u- and e-Service, Science and Technology*, 8(1):401–414, 2015.

[9] Boeing celebrates 10th anniversary of the world's best-selling satellite model. Boeing Media Room, August 2002.

[10] Stoian Borissov, Yunhe Wu, and Daniele Mortari. East–west geo satellite station-keeping with degraded thruster response. *Aerospace*, 2(4):581–601, 2015.

[11] Juan Luis Cano Rodríguez. Poliastro Documentation. website.

[12] Simone Ceccherini, Luca Ferella, and Francesco Topputo. Assessment of hybrid propulsion for geostationary transfer orbits: A mission design approach. In *67th International Astronautical Congress*, 09 2016.

[13] Jin Choi, Jung Hyun Jo, Kyoung-Min Roh, Ju-Young Son, Myung-Jin Kim, Young-Jun Choi, Hong-Suh Yim, Hong-Kyu Moon, Bang-Yeop Kim, Jang-Hyun Park, and Erricos C. Pavlis. Analysis of the angle-only orbit determination for optical tracking strategy of korea geo satellite, coms. *Advances in Space Research*, 56(6):1056–1066, 2015.

[14] Donald Chu, Sam Chen Derrick Early, Doug Freesland, Alexander Krimchansky, Bo Naasz, Alan Reth, Kumar Tadikonda, John Tsui, and Tim Walsh. GOES-R STATIONKEEPING AND MOMENTUM MANAGEMENT. In *Proceedings of the 29th ANNUAL AAS GUIDANCE AND CONTROL CONFERENCE*, Breckenridge, Colorado, February 2006. Rocky Mountain Section. Sponsored by Rocky Mountain Section.

[15] Jacob Decoto and Patrick Loerch. Technique for geo rso station keeping characterization and maneuver detection. In *Proceedings of the Advanced Maui Optical and Space Surveillance Technologies Conference (AMOS)*, 2015.

[16] P. DiBona, J. Foster, A. Falcone, and M. Czajkowski. Machine learning for RSO maneuver classification and orbital pattern prediction. In *20th Advanced Maui Optical and Space Surveillance Technologies Conference (AMOS)*, Maui, HI, 2019.

[17] Bryce Doerr, Richard Linares, and Roberto Furfaro. Space objects maneuvering prediction via maximum causal entropy inverse reinforcement learning, 2019.

[18] L. Du, Z. Zhang, X. Li, R. Wang, L. Liu, and R. Guo. Station-keeping maneuver monitoring and moving-window ground track fitting of geo satellites. *Cehui Xuebao/Acta Geodaetica et Cartographica Sinica*, 43:233–239, 03 2014.

[19] William Dupree, Louis Penafiel, and Thomas Gemmer. Time forecasting satellite light curve patterns using neural networks. In *Proceedings of the Advanced Maui Optical and Space Surveillance Technologies Conference (AMOS)*, 2021.

[20] R. Furfaro, R. Linares, D. Gaylor, M. Jah, and R. Walls. Resident Space Object Characterization and Behavior Understanding via Machine Learning and Ontology-based Bayesian Networks. In Sandy Ryan, editor, *Advanced Maui Optical and Space Surveillance Technologies Conference*, page 35, September 2016.

[21] John A. Gaebler, Penina Axelrad, and Paul W. Schumacher. Cubesat cluster deployment track initiation via a radar admissible region birth model. *Journal of Guidance, Control, and Dynamics*, 43(10):1927–1934, 2020.

[22] Gary M. Goff. *Orbit Estimation of Non-Cooperative Maneuvering Spacecraft.* PhD thesis, Air Force Institute of Technology, June 2015.

[23] José Miguel Lozano González, Catherine Praile, Sven O. Erb, Juan Manuel del Cura, Guillermo Ojeda Rodriguez, and Sven Weikert. Optimisation of ns, ew station-keeping manoeuvres for geo satellites using electric propulsion (opaskep). In *Proceedings of the 4th International Conference on Astrodynamics Tools and Techniques (ICATT)*, 2010.

[24] ISO 8601 - Date and time format. website.

[25] Terrestrial Reference Frame. GGOS website, 2020.

[26] R. Jehn, V. Agapov, and C. Hernández. The situation in the geostationary ring. *Advances in Space Research*, 35(7):1318–1327, 2005. Space Debris.

[27] Juan Luis Cano Rodríguez. pfc-uc3m. GitHub repository, 2017.

[28] Akshay Kalur, Samuel A. Szklany, and John L. Crassidis. Space object data association using spatial pattern recognition approaches. *J Astronaut Sci*, 67:1708–1734, 2020.

[29] George H. Kaplan. *The IAU Resolutions on Astronomical Reference Systems, Time Scales, and Earth Rotation Models: Explanation and Implementation.* U.S. Naval Observatory, Washington, D.C. 20392, Oct 2005. Circular No. 179.

[30] Tom Kelecy, Doyle Hall, Kris Hamada, and Dennis Stocker. Satellite maneuver detection using two-line elements data. In *Proceedings of the Advanced Maui Optical and Space Surveillance Technologies Conference (AMOS)*, 01 2007.

[31] Trent Kyono, Jacob Lucas, Michael Werth, Brandoch Calef, Ian McQuaid, and Justin Fletcher. Machine learning for quality assessment of ground-based optical images of satellites. *Optical Engineering*, 59(5):051403, 2020.

[32] Dan Lev, Roger Myers, Kristina Lemmer, Jonathan Kolbeck, Michael Keidar, Hiroyuki Koizumi, Han Liang, Daren Yu, Tony Schönherr, Jose Gonzalez del Amo, Wonho Choe, Riccardo Albertoni, Andrew Hoskins, Shen Yan, William Hart, Richard Hofer, Ikkoh Funaki, Alexander Lovtsov, Kurt Polzin, and Olivier Duchemin. The technological and commercial expansion of electric propulsion in the past 24 years. In *Proceedings of the International Electric Propulsion Conference*, 10 2017.

[33] A. Milani, Giacomo Tommei, D. Farnocchia, Alessandra Rossi, T. Schildknecht, and Rüdiger Jehn. Correlation and orbit determination of space objects based on sparse optical data. *Monthly Notices of the Royal Astronomical Society*, 417:2094–2103, 11 2011.

[34] MIT AeroAstro ARC Lab. Geosynchronous Satellite Pattern of Life Characterization. website.

[35] Rohit Mital, Kim Cates, Joe Coughlin, and Geetha Ganji. A machine learning approach to modeling satellite behavior. In *2019 IEEE International Conference on Space Mission Challenges for Information Technology (SMC-IT)*, pages 62–69, 2019.

[36] National Environmental Satellite, Data, and Information Service. How Drift Satellite: What Happens When NOAA GOES-16 is Moved to Operational Position. Website, Nov 2017.

[37] Steven R. Oleson, Roger M. Myers, Craig A. Kluever, John P. Riehl, and Francis M. Curran. Advanced propulsion for geostationary orbit insertion and north-south station keeping. Technical Report 107018, NASA Technical Memorandum, Brook Park, Ohio, July 1995.

[38] Daniel Oltrogge and Salvatore Alfano. Determination of orbit cross-tag events and maneuvers with orbit detective. In *Proceedings of AAS/AIAA Astrodynamics Specialist Conference 2011*, 08 2011.

[39] Ibrahim Oz and Ü Yılmaz. Design tradeoffs in full electric, hybrid and full chemical propulsion communication satellite. *Sakarya University Journal of Computer and Information Sciences*, 2:124–133, 12 2019.

[40] Alberto Pastor, Manuel Sanjurjo-Rivo, and David Escobar. Track-to-track association methodology for operational surveillance scenarios with radar observations. *CEAS Space J*, 2022.

[41] Alejandro Pastor, Guillermo Escribano, and Diego Escobar. Satellite maneuver detection with optical survey observations. In *Proceedings of the Advanced Maui Optical and Space Surveillance Technologies Conference (AMOS)*, 2020.

[42] Nicholas Perovich, Zachary Folcik, and Rafael Jaimes. Applications of artificial intelligence methods for satellite maneuver detection and maneuver time estimation. In *Proceedings of the Advanced Maui Optical and Space Surveillance Technologies Conference (AMOS)*, 2022.

[43] S. Pessina, P. Righetti, A. Damiano, and D. Lazaro. Analysis of Station-Keeping Manoeuvre Strategies for Meteosat Third Generation. In *Proceedings of the 25th International Symposium on Space Flight Dynamics*, 2015.

[44] Wu Qin, Heng Li Huang, Yiyi Zhang, Wang, Yan, Haiyi Xie, and Yun Cao. Precise orbit determination for beidou geo/igso satellites during orbit maneuvering with pseudo-stochastic pulses. *Remote Sensing*, 11:2587, 11 2019.

[45] Zhiwei Qin, Guanwen Huang, Qin Zhang, Le Wang, Xingyuan Yan, Yanchao Kang, Xiaolei Wang, and Shichao Xie. A method to determine beidou geo/igso orbital maneuver time periods. *Sensors*, 19:2675, 06 2019.

[46] Zhiwei Qin, Le Wang, Guanwen Huang, Qin Zhang, Xingyuan Yan, Shichao Xie, Haonan She, Fan Yue, and Xiaolei Wang. Prediction of beidou satellite orbit maneuvers to improve the reliability of real-time navigation products. *Remote Sensing*, 13:629, 02 2021.

[47] Bertrand Raffier. End of life operations for geostationary satellites. In *Proceedings of the 8th International Conference on Space Operations (SpaceOps)*, May 2006.

[48] Karina Rivera, Anthony Zara, Daniel Aguilar-Marsillach, Marcus Holzinger, Ian Elliott, and Natasha Bosanac. Patterns of Life and Maneuver Detection for Cislunar Trajectory Maintenance. In *Proceedings of the Advanced Maui Optical and Space Surveillance Technologies Conference (AMOS)*, 2021.

[49] T. G. Roberts and R. Linares. Satellite Repositioning Maneuver Detection in Geosynchronous Orbit Using Two-line Element (TLE) Data. In *71st International Astronautical Congress*, 2020.

[50] T. G. Roberts and R. Linares. Geosynchronous Satellite Maneuver Classification via Supervised Machine Learning. In *22nd Advanced Maui Optical and Space Surveillance Technologies Conference (AMOS)*, Maui, HI, 9 2021.

[51] T. G. Roberts and R. Linares. A Survey of Longitudinal-Shift Maneuvers Performed by Geosynchronous Satellites from 2010 to 2021. In *73rd International Astronautical Congress*, 2022.

[52] T. G. Roberts, H. E. Solera, and R. Linares. Geosynchronous Satellite Behavior Classification via Unsupervised Machine Learning. In *9th Space Traffic Management Conference*, Austin, TX, 3 2023.

[53] Mats Rosengren, Javier De Vicente-Olmedo, and Flemming Pedersen. Keeping Track of Geostationary Satellites – A novel and less costly approach. *ESA Bulletin*, August 2004.

[54] Joseph Saleh, Fan Geng, Michelle Ku, and Mitchell Walker. Electric propulsion reliability: Statistical analysis of on-orbit anomalies and comparative analysis of electric versus chemical propulsion failure rates. *Acta Astronautica*, 139, 07 2017.

[55] Mark Schoeberl, Carol Raymond, and Peter Hildebrand. Active and passive sensing from geosynchronous and libration orbits. Technical Report 20030093736, NASA Technical Report Server, January 2003.

[56] Romain Serra, Carlos Yanez, and Carolin Frueh. Tracklet-to-orbit association for maneuvering space objects using optimal control theory. *Acta Astronautica*, 181:271–281, 2021.

[57] Charlotte Shabarekh and Jordan Kent-Bryant. Efficient object maneuver characterization for space situational awareness. In *Proceedings of the 32nd Space Symposium*, 2016.

[58] Charlotte Shabarekh, Jordan Kent-Bryant, Gene Keselman, and Andonis Mitidis. A novel method for satellite maneuver prediction. In *Proceedings of the Advanced Maui Optical and Space Surveillance Technologies Conference (AMOS)*, 2016.

[59] J. A. Siminski, T. Flohrer, and T. Schildknecht. Assessment of post-maneuver observation correlation using short-arc tracklets. In T. Flohrer and F. Schmitz, editors, *Proceedings of the 7th European Conference on Space Debris*, Darmstadt, Germany, April 2017. ESA Space Debris Office. Ed. T. Flohrer & F. Schmitz.

[60] Jan Siminski, Hauke Fiedler, and Tim Flohrer. Correlation of observations and orbit recovery considering maneuvers. In *Proceedings of the 27th AAS/AIAA Space Flight Mechanics Meeting*, 02 2017.

[61] Mark A. Skinner, Thomas M. Kelecy, Stephen A. Gregory, Joseph P. Toth, Dennis Liang, Dean Yamanaka, Stan Kent, Rodney Tjoelker, Dragos Margineantu, Audrey L. Allison, and Christopher Heiberg. Commercial space situational awareness – an investigation of ground-based ssa concepts to support commercial geo satellite operators. In *Proceedings of the Advanced Maui Optical and Space Surveillance Technologies Conference (AMOS)*, 2013.

[62] Jean-Marc Stephan. Electric Propulsion Activities for Eurostar 3000. In R.A. Harris, editor, *Spacecraft Propulsion, Third International Conference*, number 465 in ESA SP, page 81. European Space Agency, 2001. Conference held 10-13 October, 2000 at Cannes, France.

[63] Raymond Swartz, John Coggi, and Justin McNeill. A swift sift for satellite event detection. In *Proceedings of the AIAA/AAS Astrodynamics Specialist Conference*, August 2010.

[64] Johnny L. Worthy and Marcus J. Holzinger. Incorporating uncertainty in admissible regions for uncorrelated detections. *Journal of Guidance, Control, and Dynamics*, 38(9):1673–1689, 2015.

[65] Alexandra Wright, Peter W. Boettcher, Anye Li, and Erin L. Main. Space data model modernization for proactive and machine-assisted analytics. In *Proceedings of the Advanced Maui Optical and Space Surveillance Technologies Conference (AMOS)*, 2022.

[66] Peiyuan Zhou, Lan Du, Xiaojie Li, and Yang Gao. Near real-time bds geo satellite orbit determination and maneuver analysis with reversed point positioning. *Advances in Space Research*, 63, 11 2018.